5-9-2007

Measurement of the top quark mass in the lepton+jets channel using the ideogram method

V.M. Abazov
Joint Institute for Nuclear Research, Dubna, Russia

Kenneth A. Bloom
University of Nebraska - Lincoln, kbloom2@unl.edu

D0 Collaboration

Gregory R. Snow
University of Nebraska-Lincoln, gsnow1@unl.edu

Measurement of the top quark mass in the lepton+jets channel using the ideogram method

V. M. Abazov,[35] B. Abbott,[75] M. Abolins,[65] B. S. Acharya,[28] M. Adams,[51] T. Adams,[49] E. Aguilo,[5] S. H. Ahn,[30] M. Ahsan,[59] G. D. Alexeev,[35] G. Alkhazov,[39] A. Alton,[64,*] G. Alverson,[63] G. A. Alves,[2] M. Anastasoaie,[34] L. S. Ancu,[34] T. Andeen,[53] S. Anderson,[45] B. Andrieu,[16] M. S. Anzelc,[53] Y. Arnoud,[13] M. Arov,[52] A. Askew,[49] B. Åsman,[40] A. C. S. Assis Jesus,[3] O. Atramentov,[49] C. Autermann,[20] C. Avila,[7] C. Ay,[23] F. Badaud,[12] A. Baden,[61] L. Bagby,[52] B. Baldin,[50] D. V. Bandurin,[59] P. Banerjee,[28] S. Banerjee,[28] E. Barberis,[63] A.-F. Barfuss,[14] P. Bargassa,[80] P. Baringer,[58] J. Barreto,[2] J. F. Bartlett,[50] U. Bassler,[16] D. Bauer,[43] S. Beale,[5] A. Bean,[58] M. Begalli,[3] M. Begel,[71] C. Belanger-Champagne,[40] L. Bellantoni,[50] A. Bellavance,[67] J. A. Benitez,[65] S. B. Beri,[26] G. Bernardi,[16] R. Bernhard,[22] L. Berntzon,[14] I. Bertram,[42] M. Besançon,[17] R. Beuselinck,[43] V. A. Bezzubov,[38] P. C. Bhat,[50] V. Bhatnagar,[26] M. Binder,[24] C. Biscarat,[19] G. Blazey,[52] F. Blekman,[43] S. Blessing,[49] D. Bloch,[18] K. Bloom,[67] A. Boehnlein,[50] D. Boline,[62] T. A. Bolton,[59] G. Borissov,[42] K. Bos,[33] T. Bose,[77] A. Brandt,[78] R. Brock,[65] G. Brooijmans,[70] A. Bross,[50] D. Brown,[78] N. J. Buchanan,[49] D. Buchholz,[53] M. Buehler,[81] V. Buescher,[21] S. Burdin,[50] S. Burke,[45] T. H. Burnett,[82] E. Busato,[16] C. P. Buszello,[43] J. M. Butler,[62] P. Calfayan,[24] S. Calvet,[14] J. Cammin,[71] S. Caron,[33] W. Carvalho,[3] B. C. K. Casey,[77] N. M. Cason,[55] H. Castilla-Valdez,[32] S. Chakrabarti,[17] D. Chakraborty,[52] K. Chan,[5] K. M. Chan,[71] A. Chandra,[48] F. Charles,[18] E. Cheu,[45] F. Chevallier,[13] D. K. Cho,[62] S. Choi,[31] B. Choudhary,[27] L. Christofek,[77] T. Christoudias,[43] S. Cihangir,[50] D. Claes,[67] B. Clément,[18] C. Clément,[40] Y. Coadou,[5] M. Cooke,[80] W. E. Cooper,[50] M. Corcoran,[80] F. Couderc,[17] M.-C. Cousinou,[14] S. Crépé-Renaudin,[13] D. Cutts,[77] M. Ćwiok,[29] H. da Motta,[2] A. Das,[62] G. Davies,[43] K. De,[78] P. de Jong,[33] S. J. de Jong,[34] E. De La Cruz-Burelo,[64] C. De Oliveira Martins,[3] J. D. Degenhardt,[64] F. Déliot,[17] M. Demarteau,[50] R. Demina,[71] D. Denisov,[50] S. P. Denisov,[38] S. Desai,[50] H. T. Diehl,[50] M. Diesburg,[50] A. Dominguez,[67] H. Dong,[72] L. V. Dudko,[37] L. Duflot,[15] S. R. Dugad,[28] D. Duggan,[49] A. Duperrin,[14] J. Dyer,[65] A. Dyshkant,[52] M. Eads,[67] D. Edmunds,[65] J. Ellison,[48] V. D. Elvira,[50] Y. Enari,[77] S. Eno,[61] P. Ermolov,[37] H. Evans,[54] A. Evdokimov,[36] V. N. Evdokimov,[38] A. V. Ferapontov,[59] T. Ferbel,[71] F. Fiedler,[24] F. Filthaut,[34] W. Fisher,[50] H. E. Fisk,[50] M. Ford,[44] M. Fortner,[52] H. Fox,[22] S. Fu,[50] S. Fuess,[50] T. Gadfort,[82] C. F. Galea,[34] E. Gallas,[50] E. Galyaev,[55] C. Garcia,[71] A. Garcia-Bellido,[82] V. Gavrilov,[36] P. Gay,[12] W. Geist,[18] D. Gelé,[18] C. E. Gerber,[51] Y. Gershtein,[49] D. Gillberg,[5] G. Ginther,[71] N. Gollub,[40] B. Gómez,[7] A. Goussiou,[55] P. D. Grannis,[72] H. Greenlee,[50] Z. D. Greenwood,[60] E. M. Gregores,[4] G. Grenier,[19] Ph. Gris,[12] J.-F. Grivaz,[15] A. Grohsjean,[24] S. Grünendahl,[50] M. W. Grünewald,[29] F. Guo,[72] J. Guo,[72] G. Gutierrez,[50] P. Gutierrez,[75] A. Haas,[70] N. J. Hadley,[61] P. Haefner,[24] S. Hagopian,[49] J. Haley,[68] I. Hall,[75] R. E. Hall,[47] L. Han,[6] K. Hanagaki,[50] P. Hansson,[40] K. Harder,[44] A. Harel,[71] R. Harrington,[63] J. M. Hauptman,[57] R. Hauser,[65] J. Hays,[43] T. Hebbeker,[20] D. Hedin,[52] J. G. Hegeman,[33] J. M. Heinmiller,[51] A. P. Heinson,[48] U. Heintz,[62] C. Hensel,[58] K. Herner,[72] G. Hesketh,[63] M. D. Hildreth,[55] R. Hirosky,[81] J. D. Hobbs,[72] B. Hoeneisen,[11] H. Hoeth,[25] M. Hohlfeld,[15] S. J. Hong,[30] R. Hooper,[77] P. Houben,[33] Y. Hu,[72] Z. Hubacek,[9] V. Hynek,[8] I. Iashvili,[69] R. Illingworth,[50] A. S. Ito,[50] S. Jabeen,[62] M. Jaffré,[15] S. Jain,[75] K. Jakobs,[22] C. Jarvis,[61] R. Jesik,[43] K. Johns,[45] C. Johnson,[70] M. Johnson,[50] A. Jonckheere,[50] P. Jonsson,[43] A. Juste,[50] D. Käfer,[20] S. Kahn,[73] E. Kajfasz,[14] A. M. Kalinin,[35] J. M. Kalk,[60] J. R. Kalk,[65] S. Kappler,[20] D. Karmanov,[37] J. Kasper,[62] P. Kasper,[50] I. Katsanos,[70] D. Kau,[49] R. Kaur,[26] V. Kaushik,[78] R. Kehoe,[79] S. Kermiche,[14] N. Khalatyan,[38] A. Khanov,[76] A. Kharchilava,[69] Y. M. Kharzheev,[35] D. Khatidze,[70] H. Kim,[31] T. J. Kim,[30] M. H. Kirby,[34] B. Klima,[50] J. M. Kohli,[26] J.-P. Konrath,[22] M. Kopal,[75] V. M. Korablev,[38] J. Kotcher,[73] B. Kothari,[70] A. Koubarovsky,[37] A. V. Kozelov,[38] D. Krop,[54] A. Kryemadhi,[81] T. Kuhl,[23] A. Kumar,[69] S. Kunori,[61] A. Kupco,[10] T. Kurča,[19] J. Kvita,[8] D. Lam,[55] S. Lammers,[70] G. Landsberg,[77] J. Lazoflores,[49] P. Lebrun,[19] W. M. Lee,[50] A. Leflat,[37] F. Lehner,[41] V. Lesne,[12] J. Leveque,[45] P. Lewis,[43] J. Li,[78] L. Li,[48] Q. Z. Li,[50] S. M. Lietti,[4] J. G. R. Lima,[52] D. Lincoln,[50] J. Linnemann,[65] V. V. Lipaev,[38] R. Lipton,[50] Z. Liu,[5] L. Lobo,[43] A. Lobodenko,[39] M. Lokajicek,[10] A. Lounis,[18] P. Love,[42] H. J. Lubatti,[82] M. Lynker,[55] A. L. Lyon,[50] A. K. A. Maciel,[2] R. J. Madaras,[46] P. Mättig,[25] C. Magass,[20] A. Magerkurth,[64] N. Makovec,[15] P. K. Mal,[55] H. B. Malbouisson,[3] S. Malik,[67] V. L. Malyshev,[35] H. S. Mao,[50] Y. Maravin,[59] B. Martin,[13] R. McCarthy,[72] A. Melnitchouk,[66] A. Mendes,[14] L. Mendoza,[7] P. G. Mercadante,[4] M. Merkin,[37] K. W. Merritt,[50] A. Meyer,[20] J. Meyer,[21] M. Michaut,[17] H. Miettinen,[80] T. Millet,[19] J. Mitrevski,[70] J. Molina,[3] R. K. Mommsen,[44] N. K. Mondal,[28] J. Monk,[44] R. W. Moore,[5] T. Moulik,[58] G. S. Muanza,[19] M. Mulders,[50] M. Mulhearn,[70] O. Mundal,[21] L. Mundim,[3] E. Nagy,[14] M. Naimuddin,[50] M. Narain,[77] N. A. Naumann,[34] H. A. Neal,[64] J. P. Negret,[7] P. Neustroev,[39] H. Nilsen,[22] C. Noeding,[22] A. Nomerotski,[50] S. F. Novaes,[4] T. Nunnemann,[24] V. O'Dell,[50] D. C. O'Neil,[5] G. Obrant,[39] C. Ochando,[15] V. Oguri,[3] N. Oliveira,[3] D. Onoprienko,[59] N. Oshima,[50] J. Osta,[55] R. Otec,[9] G. J. Otero y Garzón,[51] M. Owen,[44] P. Padley,[80] M. Pangilinan,[77] N. Parashar,[56] S.-J. Park,[71] S. K. Park,[30] J. Parsons,[70] R. Partridge,[77] N. Parua,[72] A. Patwa,[73] G. Pawloski,[80] P. M. Perea,[48] K. Peters,[44] Y. Peters,[25] P. Pétroff,[15] M. Petteni,[43] R. Piegaia,[1] J. Piper,[65] M.-A. Pleier,[21]

P. L. M. Podesta-Lerma,[32,†] V. M. Podstavkov,[50] Y. Pogorelov,[55] M.-E. Pol,[2] A. Pompoš,[75] B. G. Pope,[65] A. V. Popov,[38] C. Potter,[5] W. L. Prado da Silva,[3] H. B. Prosper,[49] S. Protopopescu,[73] J. Qian,[64] A. Quadt,[21] B. Quinn,[66] M. S. Rangel,[2] K. J. Rani,[28] K. Ranjan,[27] P. N. Ratoff,[42] P. Renkel,[79] S. Reucroft,[63] M. Rijssenbeek,[72] I. Ripp-Baudot,[18] F. Rizatdinova,[76] S. Robinson,[43] R. F. Rodrigues,[3] C. Royon,[17] P. Rubinov,[50] R. Ruchti,[55] G. Sajot,[13] A. Sánchez-Hernández,[32] M. P. Sanders,[16] A. Santoro,[3] G. Savage,[50] L. Sawyer,[60] T. Scanlon,[43] D. Schaile,[24] R. D. Schamberger,[72] Y. Scheglov,[39] H. Schellman,[53] P. Schieferdecker,[24] C. Schmitt,[25] C. Schwanenberger,[44] A. Schwartzman,[68] R. Schwienhorst,[65] J. Sekaric,[49] S. Sengupta,[49] H. Severini,[75] E. Shabalina,[51] M. Shamim,[59] V. Shary,[17] A. A. Shchukin,[38] R. K. Shivpuri,[27] D. Shpakov,[50] V. Siccardi,[18] R. A. Sidwell,[59] V. Simak,[9] V. Sirotenko,[50] P. Skubic,[75] P. Slattery,[71] D. Smirnov,[55] R. P. Smith,[50] G. R. Snow,[67] J. Snow,[74] S. Snyder,[73] S. Söldner-Rembold,[44] L. Sonnenschein,[16] A. Sopczak,[42] M. Sosebee,[78] K. Soustruznik,[8] M. Souza,[2] B. Spurlock,[78] J. Stark,[13] J. Steele,[60] V. Stolin,[36] D. A. Stoyanova,[38] J. Strandberg,[64] S. Strandberg,[40] M. A. Strang,[69] M. Strauss,[75] R. Ströhmer,[24] D. Strom,[53] M. Strovink,[46] L. Stutte,[50] S. Sumowidagdo,[49] P. Svoisky,[55] A. Sznajder,[3] M. Talby,[14] P. Tamburello,[45] A. Tanasijczuk,[1] W. Taylor,[5] P. Telford,[44] J. Temple,[45] B. Tiller,[24] F. Tissandier,[12] M. Titov,[22] V. V. Tokmenin,[35] M. Tomoto,[50] T. Toole,[61] I. Torchiani,[22] T. Trefzger,[23] S. Trincaz-Duvoid,[16] D. Tsybychev,[72] B. Tuchming,[17] C. Tully,[68] P. M. Tuts,[70] R. Unalan,[65] L. Uvarov,[39] S. Uvarov,[39] S. Uzunyan,[52] B. Vachon,[5] P. J. van den Berg,[33] B. van Eijk,[35] R. Van Kooten,[54] W. M. van Leeuwen,[33] N. Varelas,[51] E. W. Varnes,[45] A. Vartapetian,[78] I. A. Vasilyev,[38] M. Vaupel,[25] P. Verdier,[19] L. S. Vertogradov,[35] M. Verzocchi,[50] F. Villeneuve-Seguier,[43] P. Vint,[43] J.-R. Vlimant,[16] E. Von Toerne,[59] M. Voutilainen,[67,‡] M. Vreeswijk,[33] H. D. Wahl,[49] L. Wang,[61] M. H. L. S. Wang,[50] J. Warchol,[55] G. Watts,[82] M. Wayne,[55] G. Weber,[23] M. Weber,[50] H. Weerts,[65] A. Wenger,[22,§] N. Wermes,[21] M. Wetstein,[61] A. White,[78] D. Wicke,[25] G. W. Wilson,[58] S. J. Wimpenny,[48] M. Wobisch,[50] D. R. Wood,[63] T. R. Wyatt,[44] Y. Xie,[77] S. Yacoob,[53] R. Yamada,[50] M. Yan,[61] T. Yasuda,[50] Y. A. Yatsunenko,[35] K. Yip,[73] H. D. Yoo,[77] S. W. Youn,[53] C. Yu,[13] J. Yu,[78] A. Yurkewicz,[72] A. Zatserklyaniy,[52] C. Zeitnitz,[25] D. Zhang,[50] T. Zhao,[82] B. Zhou,[64] J. Zhu,[72] M. Zielinski,[71] D. Zieminska,[54] A. Zieminski,[54] V. Zutshi,[52] and E. G. Zverev[37]

(D0 Collaboration)

[1]*Universidad de Buenos Aires, Buenos Aires, Argentina*
[2]*LAFEX, Centro Brasileiro de Pesquisas Físicas, Rio de Janeiro, Brazil*
[3]*Universidade do Estado do Rio de Janeiro, Rio de Janeiro, Brazil*
[4]*Instituto de Física Teórica, Universidade Estadual Paulista, São Paulo, Brazil*
[5]*University of Alberta, Edmonton, Alberta, Canada,*
Simon Fraser University, Burnaby, British Columbia, Canada,
York University, Toronto, Ontario, Canada,
and McGill University, Montreal, Quebec, Canada
[6]*University of Science and Technology of China, Hefei, People's Republic of China*
[7]*Universidad de los Andes, Bogotá, Colombia*
[8]*Center for Particle Physics, Charles University, Prague, Czech Republic*
[9]*Czech Technical University, Prague, Czech Republic*
[10]*Center for Particle Physics, Institute of Physics, Academy of Sciences of the Czech Republic, Prague, Czech Republic*
[11]*Universidad San Francisco de Quito, Quito, Ecuador*
[12]*Laboratoire de Physique Corpusculaire, IN2P3-CNRS, Université Blaise Pascal, Clermont-Ferrand, France*
[13]*Laboratoire de Physique Subatomique et de Cosmologie, IN2P3-CNRS, Universite de Grenoble 1, Grenoble, France*
[14]*CPPM, IN2P3-CNRS, Université de la Méditerranée, Marseille, France*
[15]*Laboratoire de l'Accélérateur Linéaire, IN2P3-CNRS et Université Paris-Sud, Orsay, France*
[16]*LPNHE, IN2P3-CNRS, Universités Paris VI and VII, Paris, France*
[17]*DAPNIA/Service de Physique des Particules, CEA, Saclay, France*
[18]*IPHC, IN2P3-CNRS, Université Louis Pasteur, Strasbourg, France,*
and Université de Haute Alsace, Mulhouse, France
[19]*IPNL, Université Lyon 1, CNRS/IN2P3, Villeurbanne, France,*
and Université de Lyon, Lyon, France
[20]*III. Physikalisches Institut A, RWTH Aachen, Aachen, Germany*
[21]*Physikalisches Institut, Universität Bonn, Bonn, Germany*
[22]*Physikalisches Institut, Universität Freiburg, Freiburg, Germany*
[23]*Institut für Physik, Universität Mainz, Mainz, Germany*
[24]*Ludwig-Maximilians-Universität München, München, Germany*
[25]*Fachbereich Physik, University of Wuppertal, Wuppertal, Germany*
[26]*Panjab University, Chandigarh, India*

[27]Delhi University, Delhi, India
[28]Tata Institute of Fundamental Research, Mumbai, India
[29]University College Dublin, Dublin, Ireland
[30]Korea Detector Laboratory, Korea University, Seoul, Korea
[31]SungKyunKwan University, Suwon, Korea
[32]CINVESTAV, Mexico City, Mexico
[33]FOM-Institute NIKHEF and University of Amsterdam/NIKHEF, Amsterdam, The Netherlands
[34]Radboud University Nijmegen/NIKHEF, Nijmegen, The Netherlands
[35]Joint Institute for Nuclear Research, Dubna, Russia
[36]Institute for Theoretical and Experimental Physics, Moscow, Russia
[37]Moscow State University, Moscow, Russia
[38]Institute for High Energy Physics, Protvino, Russia
[39]Petersburg Nuclear Physics Institute, St. Petersburg, Russia
[40]Lund University, Lund, Sweden, Royal Institute of Technology and Stockholm University, Stockholm, Sweden, and Uppsala University, Uppsala, Sweden
[41]Physik Institut der Universität Zürich, Zürich, Switzerland
[42]Lancaster University, Lancaster, United Kingdom
[43]Imperial College, London, United Kingdom
[44]University of Manchester, Manchester, United Kingdom
[45]University of Arizona, Tucson, Arizona 85721, USA
[46]Lawrence Berkeley National Laboratory and University of California, Berkeley, California 94720, USA
[47]California State University, Fresno, California 93740, USA
[48]University of California, Riverside, California 92521, USA
[49]Florida State University, Tallahassee, Florida 32306, USA
[50]Fermi National Accelerator Laboratory, Batavia, Illinois 60510, USA
[51]University of Illinois at Chicago, Chicago, Illinois 60607, USA
[52]Northern Illinois University, DeKalb, Illinois 60115, USA
[53]Northwestern University, Evanston, Illinois 60208, USA
[54]Indiana University, Bloomington, Indiana 47405, USA
[55]University of Notre Dame, Notre Dame, Indiana 46556, USA
[56]Purdue University Calumet, Hammond, Indiana 46323, USA
[57]Iowa State University, Ames, Iowa 50011, USA
[58]University of Kansas, Lawrence, Kansas 66045, USA
[59]Kansas State University, Manhattan, Kansas 66506, USA
[60]Louisiana Tech University, Ruston, Louisiana 71272, USA
[61]University of Maryland, College Park, Maryland 20742, USA
[62]Boston University, Boston, Massachusetts 02215, USA
[63]Northeastern University, Boston, Massachusetts 02115, USA
[64]University of Michigan, Ann Arbor, Michigan 48109, USA
[65]Michigan State University, East Lansing, Michigan 48824, USA
[66]University of Mississippi, University, Mississippi 38677, USA
[67]University of Nebraska, Lincoln, Nebraska 68588, USA
[68]Princeton University, Princeton, New Jersey 08544, USA
[69]State University of New York, Buffalo, New York 14260, USA
[70]Columbia University, New York, New York 10027, USA
[71]University of Rochester, Rochester, New York 14627, USA
[72]State University of New York, Stony Brook, New York 11794, USA
[73]Brookhaven National Laboratory, Upton, New York 11973, USA
[74]Langston University, Langston, Oklahoma 73050, USA
[75]University of Oklahoma, Norman, Oklahoma 73019, USA
[76]Oklahoma State University, Stillwater, Oklahoma 74078, USA
[77]Brown University, Providence, Rhode Island 02912, USA
[78]University of Texas, Arlington, Texas 76019, USA
[79]Southern Methodist University, Dallas, Texas 75275, USA

[*]Visitor from Augustana College, Sioux Falls, SD, USA.
[†]Visitor from ICN-UNAM, Mexico City, Mexico.
[‡]Visitor from Helsinki Institute of Physics, Helsinki, Finland.
[§]Visitor from Universität Zürich, Zürich, Switzerland.

[80]*Rice University, Houston, Texas 77005, USA*
[81]*University of Virginia, Charlottesville, Virginia 22901, USA*
[82]*University of Washington, Seattle, Washington 98195, USA*
(Received 11 February 2007; published 11 May 2007)

A measurement of the top quark mass using events with one charged lepton, missing transverse energy, and jets in the final state, collected by the D0 detector from $p\bar{p}$ collisions at $\sqrt{s} = 1.96$ TeV at the Fermilab Tevatron collider, is presented. A constrained fit is used to fully reconstruct the kinematics of the events. For every event a top quark mass likelihood is calculated taking into account all possible jet assignments and the probability that an event is signal or background. Lifetime-based identification of b jets is employed to enhance the separation between $t\bar{t}$ signal and background from other physics processes and to improve the assignment of the observed jets to the quarks in the $t\bar{t}$ hypothesis. We extract a multiplicative jet energy scale (JES) factor *in situ*, greatly reducing the systematic effect related to the jet energy measurement. In a data sample with an integrated luminosity of 425 pb^{-1}, we observe 230 candidate events, with an estimated background of 123 events, and measure $m_t = 173.7 \pm 4.4(\text{stat} + \text{JES})^{+2.1}_{-2.0}(\text{syst})$ GeV. This result represents the first application of the ideogram technique to the measurement of the top quark mass in lepton+jets events.

DOI: 10.1103/PhysRevD.75.092001 PACS numbers: 14.65.Ha, 12.15.Ff

I. INTRODUCTION

The top quark is by far the heaviest known fermion. Its discovery in 1995 [1] confirmed the structure of the standard model. Its strikingly large mass highlights open questions related to the large range of quark and lepton masses and the mechanism of electroweak symmetry breaking that explains fermion masses in the theory. Within the framework of the standard model, the top quark mass is related to the Higgs boson mass and the W boson mass through radiative corrections. A precise measurement of the top quark mass helps to constrain the standard model and to predict the mass of the Higgs boson [2]. At the same time, it provides a challenge to the standard model with increased precision and distinguishes possible extensions of it.

At the Fermilab Tevatron Collider, which collides protons and antiprotons with a center-of-mass energy of 1.96 TeV, the top quark is predominantly produced in $t\bar{t}$ pairs through $q\bar{q}$ annihilation ($\approx 85\%$) and gluon-gluon fusion. In the framework of the standard model, the top quark decays almost exclusively to a b quark and a W boson. Thus, the final state topology of a $t\bar{t}$ event is determined by the decay modes of the two W bosons. The analysis presented in this paper uses the lepton+jets (ℓ+jets) channel, where one W boson decays hadronically and the other W boson decays leptonically to a muon or an electron and the corresponding (anti)neutrino. Tau leptons are not explicitly reconstructed in the analysis. Throughout this paper, charge conjugate modes are implicitly included and we use a notation with $c = 1$.

The ℓ+jets topology combines a sizable branching fraction with a striking signature of the isolated energetic lepton and large missing transverse energy from the escaping neutrino. The background consists of W+jets production and QCD multijet events with a misidentified isolated lepton and fake missing transverse energy. Reasonable signal purity can be obtained by kinematic event selection. This means that the ℓ+jets channel is particularly suited for studies of top quark properties, and it has provided the most precise measurements of the top quark mass to date [3–7].

Nonetheless, serious challenges exist. A direct measurement of the top quark mass requires that the kinematics of the event are fully reconstructed, including the momentum of the neutrino. The signal events need to be separated from backgrounds in a manner that does not bias the mass measurement. Furthermore, with four jets in the final state, the assignment of jets to the original top quark decay products gives a 12-fold ambiguity. Finally, a proper calibration of the jet energy measurement is crucial. In previous measurements, this was the dominant systematic uncertainty.

Early measurements of the top quark mass [3] (and some recent analyses [4]) used a constrained fit to reconstruct the kinematics of the event, choosing one jet assignment based on the quality of the fit. A distribution of some event variable strongly correlated to the top mass, typically the reconstructed top mass, was plotted for data events. This distribution was then compared to distributions based on a Monte Carlo simulation generated for different top quark masses to determine the value of the top quark mass that best agrees with the data. In the case of the D0 analysis [3], a multivariate discriminant that separates signal from background was also used in a two-dimensional likelihood fit to the Monte Carlo reference distributions. However, in these analyses, only a certain amount of information per event is used in the final fit.

The D0 matrix element analysis [5] demonstrated for the first time that the statistical precision of the measurement can be greatly enhanced by constructing event-by-event likelihoods that reflect the full ambiguity of the events. A

dramatic improvement was achieved, albeit at the cost of computationally intensive methods.

The analysis presented in this paper uses the ideogram technique. This method is based on a constrained kinematic fit and strives to obtain a similar improvement in statistical precision as the matrix element analysis with minimal additional computation. The constrained fit is used to determine the kinematics of the events and to improve their reconstruction beyond the detector resolution. A top quark mass likelihood is derived for every event including all possible assignments of jets to quarks in the $t\bar{t}$ hypothesis, and taking into account the possibility that the event is background. The top quark mass is extracted through a combined likelihood fit including all events. This approach is very similar to the ideogram technique used by the DELPHI experiment to measure the W boson mass at the CERN LEP collider [8]. Also there the different possible jet permutations lead to an ambiguity in the mass fit which is reflected in the event likelihood as the sum of Gaussian resolution functions. The similarity with the ideogram plots used by the Particle Data Group [9] to visualize a set of measurements is what gave the method its name. This is the first time the method is used to determine the top quark mass in the ℓ+jets channel. Recently, it has also been applied to the all-hadronic decay channel [10].

The free parameters in the fit are the top quark mass, the $t\bar{t}$ signal fraction in the sample, and an overall jet energy scale (JES) factor. Including the JES factor as a free parameter in the fit greatly reduces the systematic uncertainty related to the jet energy scale calibration [4,7]. We employ algorithms to identify jets originating from a b quark, i.e. b tagging, to enhance the separation between signal and background from other physics processes. The b tags also help to better distinguish between correct and wrong jet assignments in the likelihood. Events with and without b tags are included in the overall likelihood fit.

This paper is organized as follows: Sections II and III describe the D0 Run II detector and the event reconstruction, respectively. Sections IV, V, and VI describe the data and simulation samples used and outline the event selection. In Sec. VII, the sample composition is estimated using topological and b tagging information. Section VIII describes in detail the calculation of the ideogram likelihood and the Monte Carlo calibration procedure. The method is applied to data in Sec. IX and the systematic uncertainties are discussed in Sec. X. Section XI presents a cross-check of the JES calibration, followed by the conclusion in Sec. XII.

II. THE D0 DETECTOR

Run II of the Fermilab Tevatron collider started in 2001 after substantial detector upgrades following the first Tevatron collider run in 1992–1996. The D0 Run II detector [11] consists of a magnetic central tracking system, composed of a silicon microstrip tracker (SMT) and a central fiber tracker (CFT), both located within a 2 T superconducting solenoidal magnet. The SMT has approximately 800 000 individual strips, with typical pitch of 50–80 μm, and a design optimized for tracking and vertexing capabilities at pseudorapidities of $|\eta| < 2.5$. The system has a six-barrel longitudinal structure, each with a set of four layers arranged axially around the beam pipe, and interspersed with 16 radial disks. The CFT has eight thin coaxial barrels, each supporting two doublets of overlapping scintillating fibers of 0.835 mm diameter, one doublet being parallel to the beam axis, and the other alternating by $\pm 3^\circ$ relative to the axis. Light signals are transferred via clear fibers to solid-state photon counters (VLPCs) that have $\approx 80\%$ quantum efficiency.

Central and forward preshower detectors located just outside of the superconducting coil (in front of the calorimetry) are constructed of several layers of extruded triangular scintillator strips that are read out using wavelength-shifting fibers and VLPCs. The next layer of detection involves three liquid-argon/uranium calorimeters: a central section (CC) covering approximately $|\eta| < 1.1$, and two end calorimeters (EC) that extend coverage to $|\eta| \approx 4.2$, all housed in separate cryostats [12]. The calorimeter consists of an electromagnetic (EM) section followed by fine and coarse hadronic sections with modules assembled in a projective geometry to the interaction region. In addition to the preshower detectors, scintillators between the CC and EC cryostats provide a sampling of developing showers for $1.1 < |\eta| < 1.4$.

A muon system [13] resides beyond the calorimetry and consists of a layer of tracking detectors and scintillation trigger counters before 1.8 T iron toroids, followed by two similar layers after the toroids. Tracking for $|\eta| < 1$ relies on 10 cm wide drift tubes [12], while 1 cm minidrift tubes are used for $1 < |\eta| < 2$.

Trigger and data acquisition systems are designed to accommodate the high luminosities of Run II. Based on preliminary information from tracking, calorimetry, and muon systems, the output of the first level of the trigger is used to limit the rate for accepted events to approximately 2 kHz. At the next trigger stage, with more refined information, the rate is reduced further to about 1 kHz. These first two levels of triggering rely mainly on hardware and firmware. The third and final level of the trigger, with access to all of the event information, uses software algorithms and a computing farm, and reduces the output rate to about 50 Hz, which is written to tape.

III. EVENT RECONSTRUCTION

This section summarizes the offline event reconstruction. We use a right-handed Cartesian coordinate system with the z axis defined by the direction of the proton beam, the y axis pointing vertically upwards, and the x axis pointing out from the center of the accelerator ring. The

origin is at the center of the detector. The polar angle θ is defined with respect to the positive z axis and ϕ is the azimuthal angle from the x axis in the transverse xy plane. The pseudorapidity η is defined as $\eta \equiv -\ln(\tan(\theta/2))$.

A. Tracks and event vertex

Tracks are reconstructed from the hit information in the SMT and CFT. A Kalman filter [14] is used to fit track candidates found by a road-based algorithm or a technique searching for clusters of track parameters formed by tracker hits. Using a vertex search procedure [15], a list of reconstructed primary vertices is returned. The primary event vertex for the $t\bar{t}$ reconstruction is chosen from this list based on the p_T spectrum of the tracks associated with a given vertex. Only vertices with at least three tracks associated with them are considered.

B. Electrons

We reconstruct electrons using information from the calorimeter and the central tracker. Clusters of EM calorimeter cells (EM clusters) are built with a simple cone algorithm using seeds of $E_T > 1.5$ GeV and radius $\Delta R \equiv \sqrt{(\Delta\eta)^2 + (\Delta\phi)^2} = 0.2$. An ''extra-loose'' electron is defined as an EM cluster with 90% of its energy from the EM part of the calorimeter and isolated from hadronic energy depositions. Its longitudinal and transverse energy profiles have to be consistent with expectations from simulation. In addition, the electrons used in the final event selection are required to match a track reconstructed in the central tracker and to pass an electron likelihood cut. The likelihood is built from seven variables containing tracking and calorimeter information and is optimized to discriminate between electrons and background.

C. Muons

Muons are reconstructed from the information in the muon system and the central tracker. We require a muon candidate to have hits in the muon detectors both inside and outside the toroid. The timing information of the scintillator hits has to be consistent with that of a particle produced in a $p\bar{p}$ collision, thus rejecting cosmic muons. The muon candidate track is then extrapolated to the point of closest approach to the beam line, and matched to a track from the central tracking system using a global track fit. Muons must not be surrounded by activity in the tracker or calorimeter and are required to be separated from reconstructed jets by $\Delta R > 0.5$.

D. Jet reconstruction and energy scale

Jets are reconstructed from the calorimeter information using a cone algorithm [16] with radius $\Delta R = 0.5$. Only calorimeter cells with a signal larger than 4σ above the average noise and adjacent cells with a signal at least 2σ above the noise are used. The jets are required to be confirmed by independent calorimeter trigger information and must be separated from an extra-loose electron by $\Delta R > 0.5$. The reconstructed jet energies $E^{\text{jet}}_{\text{reco}}$ are corrected for an energy offset E_{off}, energy response R_{cal}, and out-of-cone showering C_{cone}, according to

$$E^{\text{jet}}_{\text{corr}} = \frac{E^{\text{jet}}_{\text{reco}} - E_{\text{off}}}{R_{\text{cal}} \cdot C_{\text{cone}}}. \quad (1)$$

The offset correction is determined from events taken with a zero bias trigger during physics data taking and accounts for noise, multiple interactions, and energy pileup. The response correction is derived from a high statistics jet+-photon sample by looking at the p_T imbalance in these events. The photon energy scale is assumed to be equivalent to the well-known electron energy scale as calibrated from $Z \rightarrow ee$ events. The showering correction accounts for energy that particles inside the jet cone deposit outside the cone during the hadronic showering process. Transverse jet energy profiles are studied to determine this correction. Jets containing a muon within the jet cone are further corrected for the momentum carried by the muon and the associated neutrino. Since the method to extract the top quark mass is calibrated with respect to the Monte Carlo simulation, it is important to determine the relative jet energy scale $\mathcal{S}$ between data and the Monte Carlo simulation,

$$\mathcal{S} = \left\langle \frac{p_T^{\text{jet}} - p_T^{\gamma}}{p_T^{\gamma}} \right\rangle_{\text{data}} - \left\langle \frac{p_T^{\text{jet}} - p_T^{\gamma}}{p_T^{\gamma}} \right\rangle_{\text{MC}}. \quad (2)$$

$\mathcal{S}$ is parametrized as a function of photon p_T for several bins in (p_T, η) space and is found to be flat within its uncertainties. No corrections from this source are therefore applied. Effects of a potential p_T dependence are taken into account as a systematic uncertainty. For the overall jet energy scale, a uniform factor, JES, is introduced as a free parameter in the analysis. This factor is fitted *in situ*, simultaneously with the top quark mass in data by using information from the invariant mass of the hadronically decaying W bosons. For every event, this mass is constrained in the kinematic fit to be equal to the known value of the W boson mass [9]. The χ^2 of the kinematic fit reflects the compatibility of the reconstructed jet energies with this constraint. The likelihood is sensitive to the JES parameter through the χ^2. The overall fit will give the maximum likelihood for the value of JES which optimizes, on average, the compatibility between the reconstructed and fitted jet energies.

Apart from the W boson mass information, no constraint on the overall energy scale is used in the top quark mass fit. The jet energy scale measured *in situ* is consistent with the result obtained from photon+jet studies (Sec. XI).

The analysis is calibrated such that in pseudoexperiments with Monte Carlo events the average fitted JES value is equal to one. A fitted value JES < 1 means that the jet energies in the sample considered are underestimated with

respect to the reference Monte Carlo scale described above (JES < 1 is equivalent to $\mathcal{S} < 0$ when fitting the data sample).

E. Missing transverse energy

We identify neutrinos indirectly from the energy imbalance in the event. The imbalance is reconstructed from the vector sum of the transverse energies in the calorimeter cells and the reconstructed muons. Energies from the cells in the coarse hadronic portion of the calorimeter are only added if associated with a reconstructed jet. The missing transverse energy, $\not\!\!E_T$, is corrected for the energy scale calibration of jets and electrons.

F. b-jet identification

We identify b jets using a lifetime tagging algorithm (secondary vertex tagger) based on the explicit reconstruction of a secondary vertex from the decay of a b-flavored hadron [17]. We call dca the distance of closest approach between a track and the beam line, with $\sigma(dca)$ being the uncertainty on dca. After the reconstruction of the primary event vertex, we consider tracks with $dca/\sigma(dca) > 3.5$ for the reconstruction of additional (secondary) vertices. For a reconstructed secondary vertex, the transverse decay length L_{xy} with respect to the primary event vertex is computed. A jet is tagged as a b jet if a secondary vertex is reconstructed within $\Delta R < 0.5$ of the jet with $L_{xy}/\sigma(L_{xy}) > 7.0$, where $\sigma(L_{xy})$ is the uncertainty on L_{xy}. The b-jet tagging rate ϵ_b is measured in data using information from an independent b-tagging analysis that looks for the presence of a muon in the jet cone.

Light-quark jets can also be tagged when a fake secondary vertex is reconstructed due to track mismeasurements and random overlaps of tracks. This light-jet tagging rate ϵ_l is estimated from the rate of secondary vertices with $L_{xy}/\sigma(L_{xy}) < -7.0$ in a data sample with predominantly light-quark jets. Negative values of L_{xy} occur if the secondary vertex is on the opposite side of the event vertex with respect to the jet and are a sign of mismeasurement and resolution effects. Misreconstructed vertices with negative and positive values of L_{xy} are expected to occur at the same rate. Corrections for the contamination with heavy flavor and the presence of long-lived particles are applied as determined from Monte Carlo simulation. The b-jet and light-jet tagging rates are measured in data and are parametrized as a function of jet transverse momentum and pseudorapidity [15].

IV. DATA SAMPLES

This paper describes the analysis of data collected between April 2002 and August 2004, corresponding to an integrated luminosity of approximately 425 pb^{-1}. For this analysis, the data sample was selected by triggering on a lepton and at least one additional jet in the events. The specific trigger requirements are described in more detail in Ref. [15].

The event selection requires an isolated lepton of transverse momentum $p_T > 20$ GeV, with a pseudorapidity $|\eta| < 1.1$ for electrons and $|\eta| < 2$ for muons. Missing transverse energy $\not\!\!E_T > 20$ GeV is required as well as four or more jets with $p_T > 20$ GeV and $|\eta| < 2.5$. A $\Delta\phi$ cut between $\not\!\!E_T$ and lepton momentum is imposed to exclude events where the transverse energy imbalance is caused by a poor measurement of the lepton energy. The position of the event vertex along the beam direction has to be within 60 cm of the center of the detector. We select 246 candidate events.

A QCD multijet background sample is also extracted from data by reversing the final lepton quality requirement. Leaving all other event selection cuts unchanged, the candidate isolated muon must fail to be isolated from activity in the tracker or calorimeter (Sec. III C) in the muon+jets channel. Similarly, in the electron+jets channel the candidate electron must not be matched to a track or fail to pass the electron likelihood cut (Sec. III B).

V. SIMULATION

Monte Carlo event generators are used to create large samples of simulated signal and background events. These samples are used for the calibration of the central mass value and the estimate of the uncertainty. We use ALPGEN 1.3 [18] to generate signal and W+jets background events. The underlying event and hadronization is simulated using PYTHIA 6.2 [19]. Signal $t\bar{t}$ events are generated at nine mass points with masses ranging from 150 to 200 GeV. The factorization and renormalization scales are set to $Q = m_t$ for the $t\bar{t}$ simulation and $Q^2 = M_W^2 + \sum(p_T^{\text{jet}})^2$ for W+jets. All events are passed through a full GEANT-based [20] D0 detector simulation and reconstructed with the same software as the collider data. Events are accepted according to the probability that a simulated event would pass the trigger requirements. This probability is typically between 0.9 and 1.0. The same object and event selections as for the data samples are applied. The simulation chain is tuned to reproduce resolutions of reconstructed objects seen in the collider data.

VI. KINEMATIC FIT AND FINAL EVENT SELECTION

The kinematics of the events, including the undetected neutrino from the W boson decay, are reconstructed using the same kinematic constrained fit that was developed for the Run I analysis [3]. The resolutions of muons, electrons, and jets were updated for Run II [7,21,22].

In events with more than four jets, only the four jets with highest p_T are considered as possible candidates to be a

light-quark or b quark in the $t\bar{t}$ hypothesis used in the constrained fit.

All 12 possible assignments of jets to quarks are considered. As a starting point for the kinematic fit, the unmeasured component of the neutrino momentum parallel to the beam, p_z^ν, is chosen such that the two top quarks are assigned equal mass. This yields a quadratic equation for p_z^ν. We use both solutions as input to the fit yielding 24 fit results per event. Depending on the event kinematics and resolution effects, the discriminant of the quadratic equation may be negative, in which case the discriminant is forced to be zero. Thus one or two solutions are always obtained. If only one solution is available, we include the same fit result twice in the likelihood.

For the kinematic fit, we relate the reconstructed jet energy to the unfragmented parton energy. To this end, a jet-parton energy mapping is applied, which is the same in data and MC simulation. The corrections depend on the flavor (b quark or light quark) of the parent quark and therefore depend on the jet-to-parton assignment used. To derive the mapping functions, we use MC events where the jets are unambiguously matched to the partons of the $t\bar{t}$ decay and compare the jet energy to the MC generated parton energy. The jet-parton mapping functions contain the JES parameter as a uniform multiplicative factor.

The kinematic fit is performed by minimizing a χ^2 subject to the kinematic constraints: $m(t \to \ell\nu b) = m(\bar{t} \to q\bar{q}\,\bar{b})$, $m(\ell\nu) = M_W$, and $m(q\bar{q}) = M_W$. We use $M_W = 80.4$ GeV [9]. The minimization algorithm uses the method of Lagrange multipliers; the nonlinear constraint equations are solved using an iterative technique. From the fit for each jet/neutrino solution i, we extract the fitted top quark mass m_i, the estimated uncertainty on the fitted mass σ_i, and the goodness of fit χ_i^2. The fit is repeated for different values of JES. The JES parameter is varied in steps of 3% in an interval of $\pm 15\%$ around unity. This interval was chosen to cover approximately ± 5 times the expected resolution on the JES measurement to accommodate for a test of linearity with a negligible bias due to edge effects. Only jet combinations for which the fit converges at all values of JES are used. This requirement is needed to prevent discontinuities as a function of JES in the event likelihood. The fitted mass m_i(JES), estimated uncertainty σ_i(JES), and goodness of fit χ_i^2(JES) all depend on the JES parameter. In the following this dependence is not shown explicitly, to improve readability.

The final selection requirement is that at least one jet/neutrino solution yields $\chi^2 < 10$ for the kinematic fit with JES $= 1$. This cut reduces the number of events from 120 to 116 in the electron+jets channel and from 126 to 114 in the muon+jets channel. Most of the events removed by this cut are background events or badly reconstructed $t\bar{t}$ events that do not satisfy the $t\bar{t}$ fit hypothesis and do not carry useful information about the top quark mass. The algorithmic efficiency of the kinematic fit is excellent, as listed in Table I.

TABLE I. The numbers of events and efficiencies for the electron+jets (e) and muon+jets (μ) channel having at least one jet combination for which the fit converges at JES $= 1$, without and with the requirement on the maximum value of the χ^2. The last column lists the efficiencies for the fit to converge for all values of JES in the fit range $0.85 <$ JES < 1.15. In each case the relative efficiency with respect to the previous column is shown.

Convergence of the kinematic fit:		Before fit	Converges, JES $= 1$	$\chi^2 < 10$ JES $= 1$	Converges, All JES
$t\bar{t}$	e	9452	100.0%	97.7%	100.0%
	μ	9265	99.8%	94.4%	100.0%
W+jets	e	5163	100.0%	94.2%	100.0%
	μ	5820	99.7%	89.9%	100.0%
data	e	120	100.0%	97.0%	100.0%
	μ	126	100.0%	91.0%	100.0%

VII. SAMPLE COMPOSITION

In order to obtain a good separation between $t\bar{t}$ signal and background events (mainly W+jets), a likelihood discriminant based on the ''low-bias'' topological discriminant $D_{\rm LB}$, developed in Run I [3], is used. The $D_{\rm LB}$ discriminant was designed to have minimal correlation with the top mass and is based on the following four topological variables: $\not\!\!E_T$, aplanarity, H'_{T2}, and $K'_{T\,\rm min}$. Aplanarity is defined as the smallest eigenvalue of the normalized laboratory-frame momentum tensor of the jets and the W boson. $H'_{T2} \equiv H_{T2}/H_{\|}$ measures the event centrality, where H_{T2} is the scalar sum of the transverse momenta of the jets excluding the leading jet and $H_{\|}$ is the sum of the magnitudes of the momentum components parallel to the beam line of the jets, isolated lepton, and neutrino. In this case the neutrino momentum parallel to the beam is estimated requiring that the mass computed from the measured lepton momentum, $\not\!\!E_T$ and unknown neutrino momentum parallel to the beam is equal to the W boson mass. If more than one solution is found, the one smallest in absolute value is used. The variable $K'_{T\,\rm min} \equiv (\Delta R_{ij}^{\rm min} \cdot E_T^{{\rm lesser}\,j})/(E_T^W)$ is a measure of the jet separation normalized by the transverse energy of the reconstructed W boson. $\Delta R_{ij}^{\rm min}$ is the smallest distance in $\eta - \phi$ space between any two of the four leading jets. $E_T^{{\rm lesser}\,j}$ is the smaller of the two jet E_Ts. The transverse energy of the W boson is defined as $E_T^W \equiv |p_T^{\rm lepton}| + |\not\!\!E_T|$. These four variables are combined in a single discriminant variable $D_{\rm LB}$ using the likelihood ratio procedure described in Ref. [3].

For the analysis presented here, the low-bias discriminant $D_{\rm LB}$ ($\equiv x_1$) was combined with a new variable called ''p_T-fraction'' and the number of b tags to build a combined discriminant D. The p_T-fraction, defined as

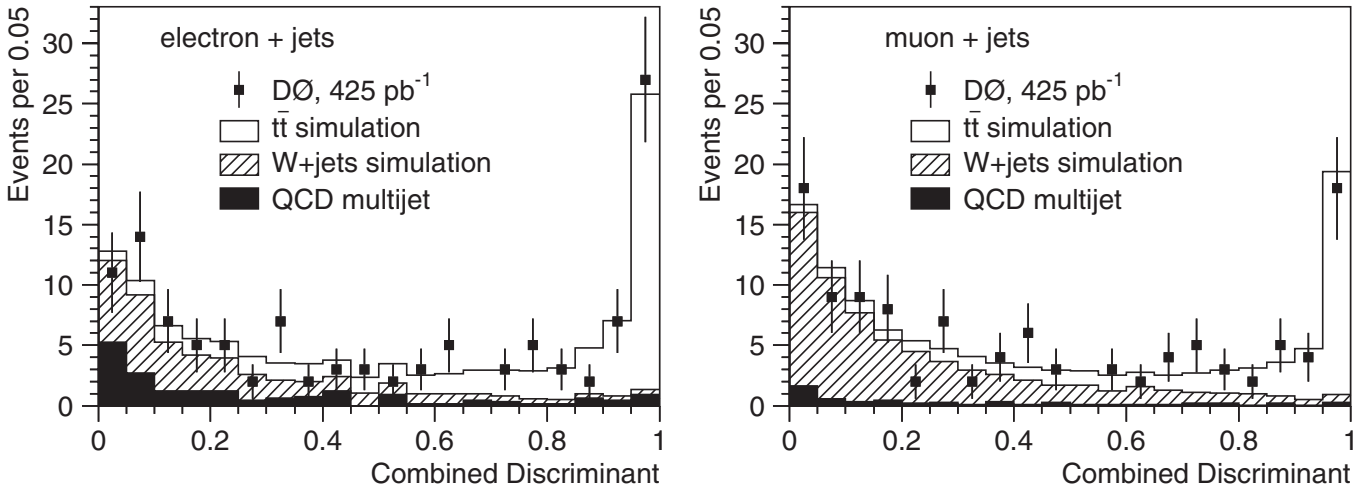

FIG. 1. Combined likelihood discriminant D in data and MC simulation in the electron+jets channel (left) and muon+jets channel (right). The $t\bar{t}$, W+jets, and multijet contributions are normalized according to the fitted fractions.

$x_2 = (\sum_{\text{tracks in jets}} p_T)/(\sum_{\text{all tracks}} p_T)$, is the p_T-weighted fraction of all tracks in the event that point to an energy deposit defining a jet (with jet $p_T > 20$ GeV with $|\eta| < 2.5$). Only those tracks were considered that have a distance of closest approach of less than 1 cm along the beam direction with respect to at least one of the primary vertices in the event. In order to be included in the p_T sum over tracks in a jet, a track was required to be within $\Delta R < 0.5$ from the jet axis. This variable distinguishes clean events with nicely collimated jets from events with broader jets and significant underlying hadronic activity. Finally, x_3 is the number of b tags. For each variable x_i, we use Monte Carlo simulation to determine the probability density functions s_i, for $t\bar{t}$ signal, and b_i, for W+jets background. To a good approximation, these three variables x_i are uncorrelated, and the combined likelihood discriminant is derived as

$$D = \frac{\Pi_i[s_i(x_i)/b_i(x_i)]}{\Pi_i[s_i(x_i)/b_i(x_i)] + 1}, \tag{3}$$

thus combining event topology with a tracking-based jet shape and b tag information. This combined likelihood discriminant offers a much better discrimination between $t\bar{t}$ and background than does the low-bias topological variable D_{LB} by itself, while maintaining its low level of correlation with the fitted top quark mass (and therefore with the jet energy scale).

TABLE II. Composition of the 425 pb^{-1} data sample as determined by the likelihood fit.

	electron+jets	muon+jets
$t\bar{t}$	61.5 ± 7.9	45.6 ± 7.5
W+jets	35.6 ± 5.2	63.0 ± 6.9
QCD multijet	18.9 ± 2.7	5.4 ± 0.6
Total observed	116	114

Figure 1 shows the distribution of the combined discriminant D obtained in the electron+jets and muon+jets channels. The distribution observed in data is compared to a model consisting of simulated $t\bar{t}$ and W + jets events and the QCD multijets sample obtained from data (Sec. IV). A likelihood fit is performed to determine the estimated fraction of $t\bar{t}$ events. The fit results are shown in Table II. In the fit, the ratio between the number of QCD and W+jets events was kept fixed at a value based on the estimate used in Refs. [7,23].

VIII. THE IDEOGRAM METHOD

To maximize the statistical information on the top quark mass extracted from the event sample, a likelihood to observe the event is calculated for each event as a function of the assumed top quark mass m_t, the jet energy scale parameter JES, and the fraction of $t\bar{t}$ events in the event sample, f_{top}. The likelihood is composed of two terms, describing the hypotheses that the event is $t\bar{t}$ signal or background:

$$\mathcal{L}_{\text{evt}}(x; m_t, \text{JES}, f_{\text{top}}) = f_{\text{top}} \cdot P_{\text{sgn}}(x; m_t, \text{JES}) + (1 - f_{\text{top}}) \cdot P_{\text{bkg}}(x; \text{JES}). \tag{4}$$

Here, x denotes the full set of observables that characterizes the event, f_{top} is the signal fraction of the event sample, and P_{sgn} and P_{bkg} are the probabilities for $t\bar{t}$ and W+jets production, respectively. The contribution from QCD multijet events is comparatively small and expected to have a fitted mass shape very similar to that of W+jets events. Therefore no explicit QCD multijet term is included in the likelihood. The event observables x can be divided into two groups. One set is chosen to provide good separation between signal and background events while

minimizing the correlation with the mass information in the event. These variables (topological variables and b tagging) are used to construct a low-bias combined discriminant D, as described in Sec. VII. The other event information used is the mass information $x_{\rm fit}$ from the constrained kinematic fit, which provides the sensitivity to the top quark mass and jet energy scale. To good approximation D is uncorrelated with $x_{\rm fit}$ and with the jet energy scale. Thus the probabilities $P_{\rm sgn}$ and $P_{\rm bkg}$ can be written as the product of a probability to observe a value D and a probability to observe $x_{\rm fit}$, as

$$P_{\rm sgn}(x; m_t, \mathrm{JES}) \equiv P_{\rm sgn}(D) \cdot P_{\rm sgn}(x_{\rm fit}; m_t, \mathrm{JES}) \quad (5)$$

and

$$P_{\rm bkg}(x; \mathrm{JES}) \equiv P_{\rm bkg}(D) \cdot P_{\rm bkg}(x_{\rm fit}; \mathrm{JES}), \quad (6)$$

where D is calculated for a JES parameter equal to 1. The normalized probability distributions of the discriminant D for signal $P_{\rm sgn}(D)$ and background $P_{\rm bkg}(D)$ are assumed to be independent of JES and are obtained from Monte Carlo simulation as discussed in Sec. VII. They correspond to parametrized versions of the Monte Carlo templates shown in Fig. 1. The reconstruction of the signal and background probabilities for the mass information $x_{\rm fit}$ is explained in Sec. VIII A. The mass information in the event $x_{\rm fit}$ consists of all fitted masses m_i(JES), estimated uncertainties σ_i(JES), and goodnesses-of-fit χ^2_i(JES) obtained from the kinematic fit.

A. Calculation of signal and background probability

The signal and background probabilities are calculated as a sum over all 24 possible jet/neutrino solutions. Without b tagging, the relative probability for each of the solutions i to be correct depends only on the χ^2_i for the corresponding fit and is proportional to $\exp(-\frac{1}{2}\chi^2_i)$. To further improve the separation between correct and incorrect jet assignments, b tagging is used. If one or more jets in the event are b tagged, an additional relative weight $w_{\mathrm{btag},i}$ is assigned, representing the probability that the observed b tags are compatible with the jet assignment assumed for that particular jet permutation:

$$w_{\mathrm{btag},i} = \prod_{j=1,n_{\rm jet}} p^j_i, \quad (7)$$

where p^j_i can either be ε_l, $(1-\varepsilon_l)$, ε_b, or $(1-\varepsilon_b)$, depending on the assumed flavor of the jet (light or b) and whether or not that particular jet is tagged. For this purpose the jets from the hadronic W boson decay are always assumed to be light-quark (u, d, s) jets. In the calibration of the analysis (see Sec. VIII E), however, the fraction of $W \to c\bar{s}$ decays and the higher tagging rate for c quark jets are taken into account. The tagging rates for light and b quark jets ε_l and ε_b are used as parametrized functions of jet p_T and η. The jet p_T is based on the reconstructed jet energy for JES $= 1$, consistent with the jet energy scale for which the tagging rate functions are derived from data [17]. Thus, the weight assigned to each jet combination becomes

$$w_i = \exp(-\tfrac{1}{2}\chi^2_i) \cdot w_{\mathrm{btag},i}. \quad (8)$$

The mass-dependent signal probability in Eq. (5) is calculated as

$$P_{\rm sgn}(x_{\rm fit}; m_t, \mathrm{JES}) \equiv \sum_{i=1}^{24} w_i \Big[f^{\rm ntag}_{\rm correct} \cdot \int_{m_{\rm min}}^{m_{\rm max}} \mathbf{G}(m_i, m', \sigma_i) \cdot \mathbf{BW}(m', m_t) dm' + (1 - f^{\rm ntag}_{\rm correct}) \cdot S^{\rm ntag}_{\rm wrong}(m_i, m_t) \Big]. \quad (9)$$

The signal term consists of two parts: one part describes the compatibility of the solution with a certain value of the top quark mass, assuming that it is the correct solution. It takes into account the estimated mass resolution σ_i for each jet permutation. The second part of the signal term describes the expected shape of the mass spectrum for the "wrong" jet assignments, which also depends on the top quark mass. The "correct" solution part is given by a convolution of a Gaussian resolution function $\mathbf{G}(m_i, m', \sigma_i)$ and a relativistic Breit-Wigner $\mathbf{BW}(m', m_t)$. The Gaussian function describes the experimental resolution. The relativistic Breit-Wigner represents the expected distribution of the average invariant mass m' of the top and antitop quark in the event for a given top quark mass m_t. The width of the Breit-Wigner is set to the standard model value of the top decay width [9]. The wrong permutation signal shape $S^{\rm ntag}_{\rm wrong}(m_i, m_t)$ is obtained from MC simulation using a procedure described in Sec. VIII B. These two terms are assigned relative weights depending on $f^{\rm ntag}_{\rm correct}$, which represents the relative probability that the weight is assigned to the correct jet permutation. For well-reconstructed events with exactly 4 jets, this probability is approximately 39% if b tagging is not used. For 4-jet events with 0, 1, or ≥ 2 tagged jets, the values $f^0_{\rm correct} = 0.45$, $f^1_{\rm correct} = 0.55$, and $f^2_{\rm correct} = 0.65$ are used. For 5-jet events smaller fractions are used: 0.15, 0.30, and 0.40 for events with 0, 1, or ≥ 2 b tagged jets, respectively. Ensemble tests (see Sec. VIII E) confirm that these values result in a pull width for the mass close to unity for the different tagging multiplicities.

The background term in Eq. (6) is calculated as

$$P_{\rm bkg}(x_{\rm fit}; \mathrm{JES}) \equiv \sum_{i=1}^{24} w_i \cdot BG(m_i), \quad (10)$$

where the background shape $BG(m)$ is the shape of the fitted mass spectrum for W+jets events. To obtain $BG(m)$, the kinematic fit (with JES equal to unity) is applied to simulated W+jets events and the fitted masses m_i for all possible jet/neutrino solutions i are plotted. All entries are weighted according to the permutation weight w_i defined

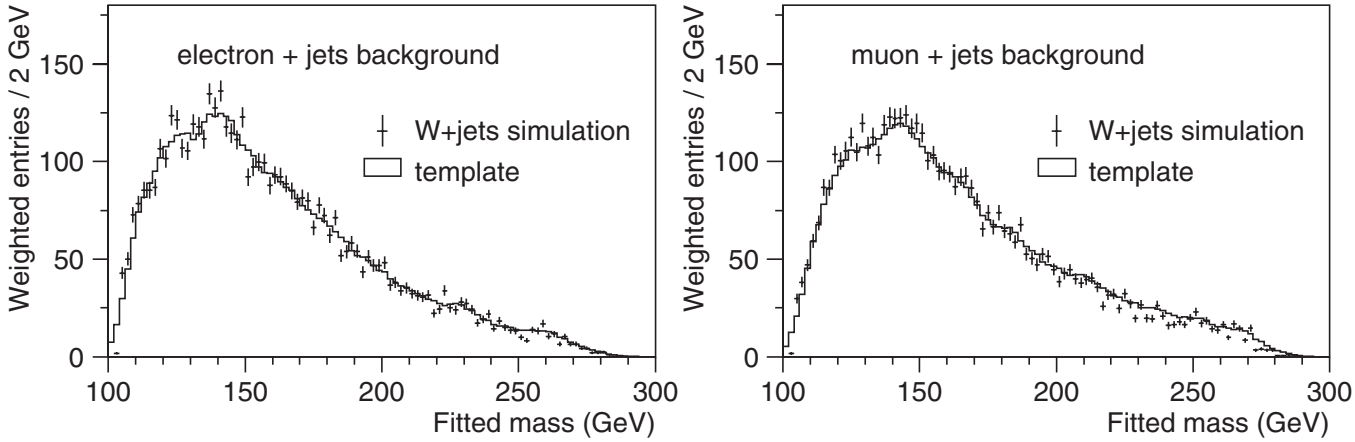

FIG. 2. Histograms showing the background shape from a weighted sum (see text) of all 24 masses from each event from the W+jets background sample (points with error bars), for the electron+jets channel (left) and muon+jets (right). The histograms show the shapes that are used in the likelihood. To reduce statistical fluctuations, the shapes are calculated as the average value in a sliding window of ± 5 GeV around each fitted mass.

in Eq. (8). The shapes of $BG(m)$ used in the analysis are shown in Fig. 2.

The Breit-Wigner and wrong permutation signal shape are normalized to unity within the integration interval of $m_{\mathrm{min}} = 100$ GeV to $m_{\mathrm{max}} = 300$ GeV. This interval is chosen to be large enough so as not to bias the mass in the region of interest.

The normalization of the background shape $BG(m)$ is chosen such that the fitted signal fraction f_{top} reproduces the true $t\bar{t}$ fraction in ensemble tests (see Sec. VIII E) containing $t\bar{t}$ and W+jets events. The mass fit tends to underestimate f_{top}, due to the presence of $t\bar{t}$ events that are misreconstructed or affected by energetic gluon radiation and resemble W+jets events in the fact that their topology does not conform to the $t\bar{t}$ hypothesis in the kinematic fit. A constant normalization factor of 1.15 is found to reduce the offset in f_{top} to less than 1% both in the electron+jets and the muon+jets channel. The jet energy scale parameter is varied before performing the constrained fit by scaling all jet energies by a constant factor. The event likelihoods are recalculated for each different value of the JES parameter. Since the constrained fit uses a W boson mass constraint, the χ^2 in the fit will be best when the invariant mass of the jets from the hadronically decaying W boson is closest (on average) to the known W boson mass. Additional sensitivity to the jet energy scale comes from the shape of the fitted mass distribution in background events. For the proper jet energy scale the spectrum will agree best with the background shape included in the background term in the likelihood.

B. Determination of the wrong-permutation signal shape

The convolution of Gaussian detector resolution and a Breit-Wigner, used in the signal term of the likelihood, implicitly assumes that the correct jet assignment is chosen. To describe the contribution from wrong jet assignments, a separate term is added to the signal part of the likelihood. To obtain the fitted mass spectrum of the wrong-permutation signal, samples of parton-matched $t\bar{t}$ events are used in which all quarks are matched to jets. The fitted mass spectrum is plotted including all jet permutations *except* the correct solution (excluding both neutrino solutions corresponding to the correct jet permutation). Each entry is weighted according to the permutation weight assigned in the ideogram likelihood. Samples of

TABLE III. Parameters used to describe the background shapes (arbitrary normalization). For each case, the shape is described by the sum of two Gaussians $G(m_{\mathrm{fit}}) = a \cdot \exp[-(\mu - m_{\mathrm{fit}})^2/2\sigma^2]$, where the three parameters a, μ, and σ evolve linearly as a function of the generated top quark mass m_t as $p0 + p1 \cdot (m_t - 175\ \mathrm{GeV})$.

	0 tags				1 tag				≥ 2 tags			
	Gaussian 1		Gaussian 2		Gaussian 1		Gaussian 2		Gaussian 1		Gaussian 2	
Parameter	$p0$	$p1$	$p0$	$p1$	$p0$	$p1$	$p0$	$p1$	$p0$	$p1$	$p0$	$p1$
a	284.9	−1.722	51.72	−0.4199	267.5	−1.0700	68.08	−0.7129	235.5	−0.1662	75.86	−0.0415
μ	161.7	0.7383	223.1	1.242	162.6	0.7859	220.1	1.400	166.2	0.6416	229.4	0.7454
σ	23.55	0.2392	22.94	−0.2528	23.27	0.2737	23.97	−0.4551	25.80	0.1165	21.78	−0.2828

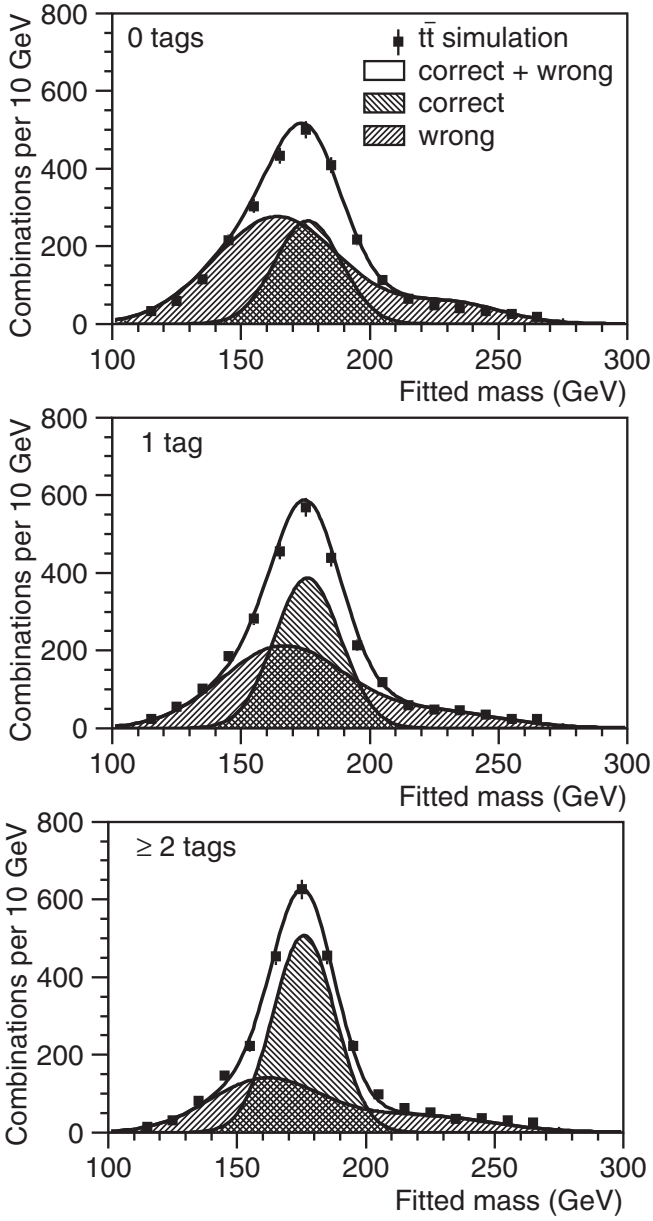

FIG. 3. Prediction of the shapes of the fitted mass distribution for the wrong and the correct permutations (hatched) and the sum of the two (black line) using the fitted parameters shown in Table III. The sum of the two is compared to the simulated data containing a weighted sum of all solutions (correct and wrong), for the default jet energy scale and a generated top quark mass of 175 GeV for events with 0 (top), 1 (middle), or more than 1 (bottom) b tags.

different generated top quark masses are used. For each mass, the weighted sum of wrong solutions is fitted with a double Gaussian. The fitted parameters for correct solutions and for the wrong-permutation signal show a linear behavior as a function of the top quark mass. The fitted parameters are given in Table III. Since the permutation weights change when b tagging is included, this exercise is repeated for events with 0 tags, 1 tag, and 2 or more tags.

The linear fits are used to construct a 2-dimensional wrong-permutation signal shape as a function of the fit mass and generated top quark mass $S^{\mathrm{ntag}}_{\mathrm{wrong}}(m_i, m_t)$. For each value of the generated top quark mass, the shape as a function of fitted mass is described as the sum of two Gaussians. The resulting parametrizations are displayed as the wrong-permutation shapes in Figs. 3 and 4. Also shown are the shapes of the correct jet assignments, determined in a similar fashion from parton-matched events using a single Gaussian. A linear dependence of the parameters is found as a function of generated top quark mass. The sum of the correct solutions and wrong solutions is compared to a weighted histogram of all fitted masses in $t\bar{t}$ simulation. The parametrized functions give an adequate description of the overall (wrong+correct) signal shape. In Fig. 3, the corresponding distributions are shown for events with 0, 1, or 2 tags. It is clearly visible how the fraction of the weight given to the correct solution improves when including b tag information in the permutation weights. In Fig. 4, the nine distributions are shown for generated top quark masses ranging from 150 to 200 GeV.

C. Determination of JES offset correction

The likelihood fit relies on the invariant mass of the hadronically decaying W boson in the $t\bar{t}$ events to set the jet energy scale. It is designed to give an unbiased fit of the JES parameter in well-reconstructed $t\bar{t}$ events when the correct jet assignment is used. However, in a significant fraction of the events, the jets that are presumed to originate from the W boson may not really come from a W boson. Such cases include events other than $t\bar{t}$, as well as $t\bar{t}$ events that are misreconstructed. In the presence of such events we can expect an offset in the fitted JES parameter. The slope of the JES calibration curve (fitted JES parameter as a function of the ''true'' JES) may also differ from unity.

Using the MC calibration procedure described in Sec. VIII E, we find that the presence of wrong jet assignments and background events causes an offset of several percent in the fitted JES parameter. A breakdown of the different contributions to the JES offset and slope is shown in Table IV.

The JES offset and slope turn out to be independent of the generated top quark mass (see Fig. 5). Therefore we apply a straightforward mass-independent correction. A normalization factor $f_{\mathrm{JES}}(\mathrm{JES}, f_{\mathrm{top}}) = \exp(a/\mathrm{JES})$ is introduced which corrects for the offset without changing the statistical uncertainty estimated from the likelihood (in case the final sample likelihood is Gaussian and JES is close to 1):

$$\mathcal{L}^{\mathrm{corr}}_{\mathrm{evt}}(m_t, \mathrm{JES}, f_{\mathrm{top}}) = f_{\mathrm{JES}}(\mathrm{JES}, f_{\mathrm{top}}) \cdot \mathcal{L}_{\mathrm{evt}}(m_t, \mathrm{JES}, f_{\mathrm{top}}). \quad (11)$$

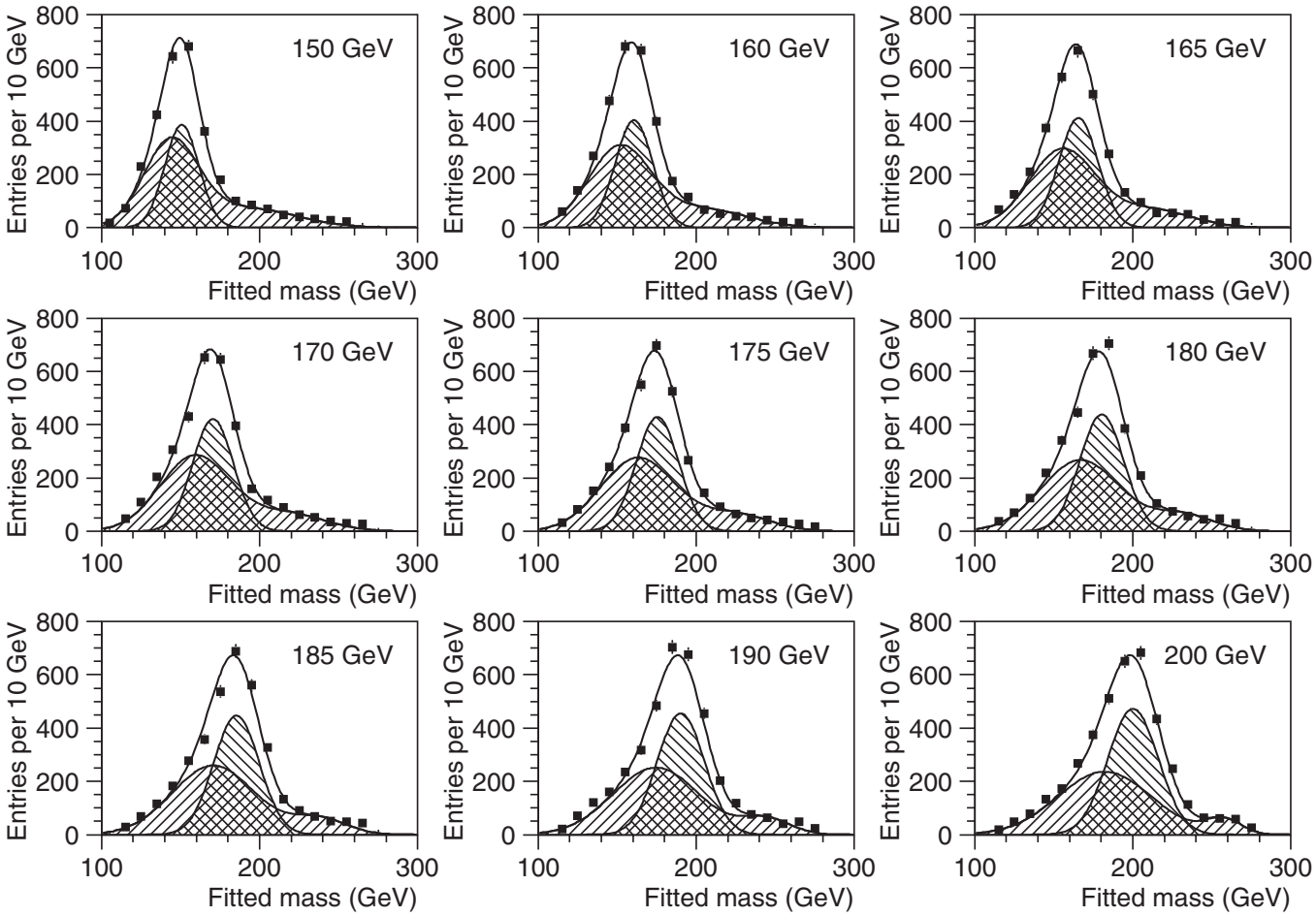

FIG. 4. Same as Fig. 3, for different values of the generated top quark mass, combining all events irrespective of the number of b tags.

Since background events on average cause a larger bias than signal events, a is defined to be dependent on the measured signal fraction f_{top}: $a = 2.63 + 0.56(1 - f_{\text{top}})$. The value of the correction constant is tuned using MC simulation to give an unbiased measurement of the JES at the reference scale JES = 1. As shown in Table IV, the application of this offset correction removes the JES offset, but it further reduces the JES calibration slope. Table IV also shows that, after full calibration (described in the next section), the expected statistical uncertainty on the top quark mass improves slightly when applying the corrections. For illustrative purposes we also include a 50% offset correction in the table, where $0.5 \cdot a$ is used instead of a.

TABLE IV. The JES calibration slope and offset for different event samples are shown. The offset increases and the calibration slope becomes smaller when misreconstructed signal events or background events are added. The offset correction at the likelihood level (see text) fixes the JES offset but further reduces the JES calibration slope. The expected mass uncertainty δm_t is determined after full calibration.

	JES slope	JES offset	δm_t
Parton-matched $t\bar{t}$ only	0.96	+0.026	
$t\bar{t}$ only	0.88	+0.050	
All events	0.80	+0.076	4.30 GeV
All, 50% offset correction	0.72	+0.036	4.10 GeV
All, 100% offset correction	0.63	+0.000	4.01 GeV

The correction described above ensures that the fit is well behaved and that, for values of the JES parameter near 1, the fit results will stay well within the range for which the (JES, m_t) likelihood is calculated. It does not, however, provide a full calibration of the analysis, which is described in Sec. VIII E.

D. Combined likelihood fit

Since each event is independent, the combined likelihood for the entire sample is calculated as the product of the single event likelihood curves:

$$\mathcal{L}_{\text{samp}}(m_t, \text{JES}, f_{\text{top}}) = \prod_j \mathcal{L}^{\text{corr}}_{\text{evt}j}(m_t, \text{JES}, f_{\text{top}}). \quad (12)$$

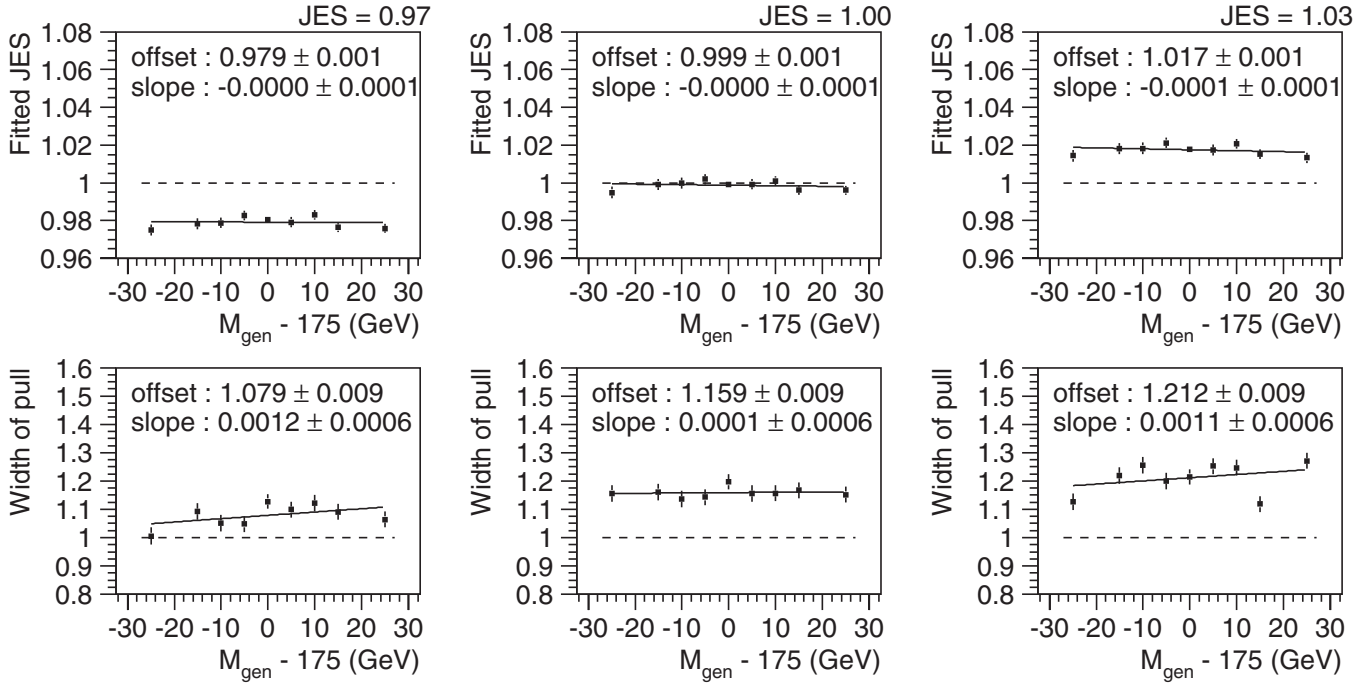

FIG. 5. The mean fitted JES and pull width as a function of the generated top quark mass M_{gen} for a true JES of 0.97 (left), 1.00 (middle), and 1.03 (right), for the lepton+jets channel ($e + \mu$ combined). The fitted JES is stable as a function of generated top quark mass.

This likelihood is maximized with respect to the top quark mass m_t, the jet energy scale parameter JES, and the estimated fraction of signal in the sample f_{top}.

E. Calibration using Monte Carlo simulation

The analysis is calibrated using Monte Carlo simulation. Both the bias on the measured mass and the correctness of the estimated statistical uncertainty are studied using ensemble tests, in which many simulated experiments (pseudoexperiments) are created, each matching the size of the observed data sample. A typical ensemble consists of a thousand pseudoexperiments, constructed using $t\bar{t}$ and W+jets events from MC simulation. The event fractions for $t\bar{t}$ and W+jets are allowed to fluctuate according to binomial statistics around the estimated fractions in the actual data sample. The fractions used are those listed in Table II. In the pseudoexperiments, the QCD multijets contribution is replaced by W+jets events. This deviation in QCD multijet fraction is treated as a systematic uncertainty (see Sec. X). The total sample size is fixed to the observed number of events in data (116 in electron+jets and 114 in muon+jets). To make optimal use of the available MC statistics, standard resampling techniques are used, allowing for the multiple use of MC events when constructing the pseudoexperiments [24]. For every pseudoexperiment the mass is fitted and the deviation of this mass from the mean of all pseudoexperiment masses is divided by the fitted uncertainty. This quantity is referred to as the "pull." The pull distribution for all pseudoexperiments is fitted with a Gaussian to extract the width, which we call the "pull width." The corresponding pull and pull width for the fitted JES are also determined.

Figure 5 shows how the mean fitted JES and its pull width behave as a function of the top quark mass for different values of the true jet energy scale. The fitted JES parameter is independent of the top quark mass over the full range considered. The plots also show that the fitted JES changes linearly as a function of the true JES with a slope of 0.63 (see discussion in Sec. VIII C). Figure 6 shows the change in the fitted top quark mass and the width of the pull as a function of the generated top quark mass for different values of the true JES. Using these plots a full two-dimensional calibration is performed, describing the fitted JES and top quark mass as a function of the true JES and top quark mass generated in the MC simulation. We derive the calibration of the JES measurement from Fig. 5. This calibration is independent from the top quark mass, as demonstrated by the slope parameter in Fig. 5. The mass measurement is calibrated from the fits shown in Fig. 6 and the corrected JES. The relation between fitted and generated mass as a function of generated JES is obtained by a linear fit to the offset and slope parameters. The estimated statistical uncertainties are corrected for the width of the pull and error propagation is used to take into account the effect of the full calibration procedure, including the correlation between the JES parameter and the offset in measured mass.

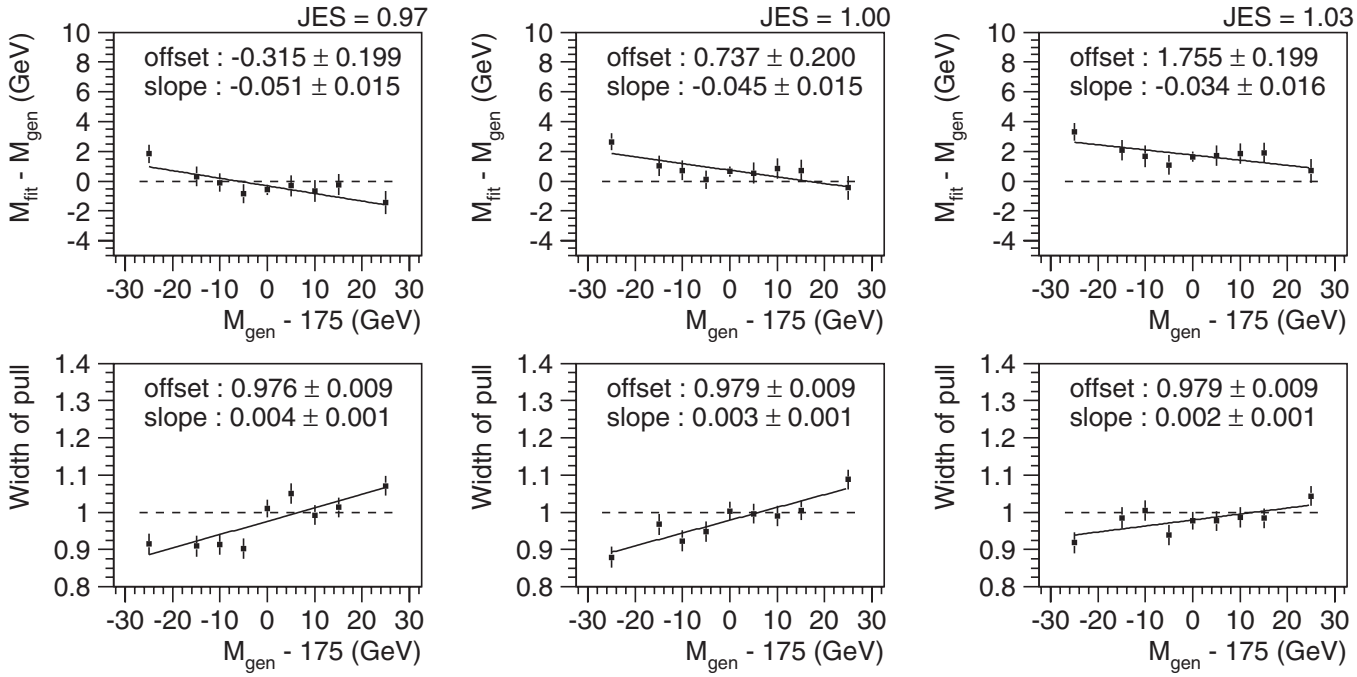

FIG. 6. The difference between the mean fitted mass M_{fit} and the generated top quark mass M_{gen} as a function of the generated top quark mass for a true JES of 0.97 (left), 1.00 (middle), and 1.03 (right), for the lepton+jets channel ($e + \mu$ combined). At a generated mass of 175 GeV, the mass bias changes by 1 GeV when the true JES is varied by $\pm 3\%$.

F. Alternative JES fitting strategies

Including the uniform JES parameter as a free parameter in the fit reduces the systematic uncertainty due to the jet energy scale, at the cost of a larger statistical uncertainty. As a comparison, in Fig. 7 the expected statistical uncertainties on the top quark mass are shown for three different fitting scenarios. When fixing the JES parameter in the fit to 1, the statistical uncertainty is smallest: 2.59 GeV at a generated top quark mass of 175 GeV. When allowing the JES parameter to float freely in the fit, without correcting for the JES slope (= 0.63) in the calibration, part of the sensitivity to the overall JES scale is reduced and absorbed in the statistical uncertainty, leading to an expected statistical uncertainty of 3.34 GeV at a top quark mass of 175 GeV. Fully calibrating the analysis as a function of fitted mass and JES (the default approach) allows an unbiased top quark mass measurement for any value of the true JES, at the cost of a larger statistical uncertainty: 4.01 GeV at a generated top quark mass of 175 GeV.

In order to be consistent with the approach used by the matrix element analysis [7], thus facilitating a combination of results, and to minimize the dependence on the external JES constraint from jet+photon studies, the third scenario is presented here as the main analysis result, applying the

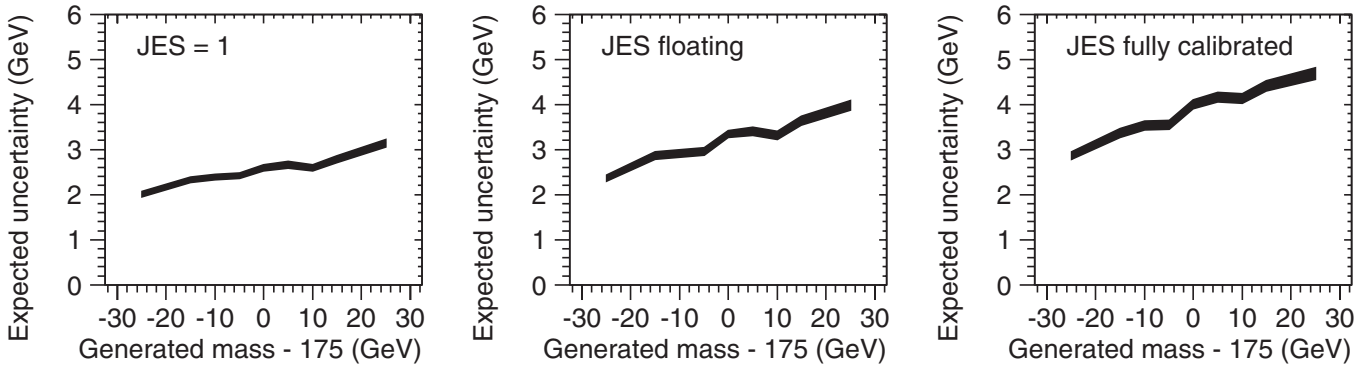

FIG. 7. The expected statistical uncertainty from ensemble tests is shown as a function of the generated top quark mass for three scenarios: with the JES parameter fixed to 1 (left), allowing the JES parameter to float freely in the fit, but only calibrating the mass fit for a true JES = 1 (middle), allowing the JES parameter to float freely in the fit and applying the full calibration as a function of true top quark mass and true JES (right). In each plot the width of the band indicates the estimated uncertainty.

full calibration as a function of fitted top quark mass and JES. Results using the other two JES fitting strategies are quoted as a cross-check in Sec. XI.

IX. RESULTS WITH DATA

The overall likelihood curves obtained for data are shown in Fig. 8. The 2D likelihoods show the actual likelihood values in bins of 1 GeV in mass and 3% in JES. The jagged appearance of the ellipses is caused by the large bin size in the JES direction. To extract the mass and statistical error, a Gaussian fit is applied to the three bins closest to the minimum in the one-dimensional negative log likelihood curves. The fitted values are corrected according to the calibration derived in Sec. VIII E. The measured top quark mass is

$$m_t = 173.7 \pm 4.4(\text{stat} + \text{JES})\ \text{GeV} \quad \text{with}$$
$$\text{JES} = 0.989 \pm 0.029(\text{stat}).$$

All uncertainties shown are statistical. The fitted $t\bar{t}$ signal fraction is $f_{\text{top}} = 0.453 \pm 0.032$. If the JES parameter is kept fixed to 1 in the fit, the estimated statistical uncertainty is 2.93 GeV. Hence the 4.43 GeV (stat + JES) uncertainty of the 2D fit can be interpreted as a combination of an intrinsic mass uncertainty of 2.93 GeV (stat) and an additional uncertainty of 3.32 GeV (JES) due to fitting the JES parameter. As shown in Fig. 9, the observed statistical uncertainties are slightly larger than the average uncertainties expected from Monte Carlo ensemble tests, but they fall well within the distribution. The fitted JES of 0.989 ± 0.029 is in good agreement with the reference scale 1 (or $\mathcal{S} = 0$), corresponding to the hypothesis that after all jet corrections the JES in data and MC are the same.

One can also compare the *in situ* fitted JES parameter with the scale obtained in jet+photon studies. When correcting all jets in MC events for the jet-p_T dependent difference between data and MC, $\mathcal{S}$, and redoing the ensemble tests in MC simulation, the mean fitted JES is

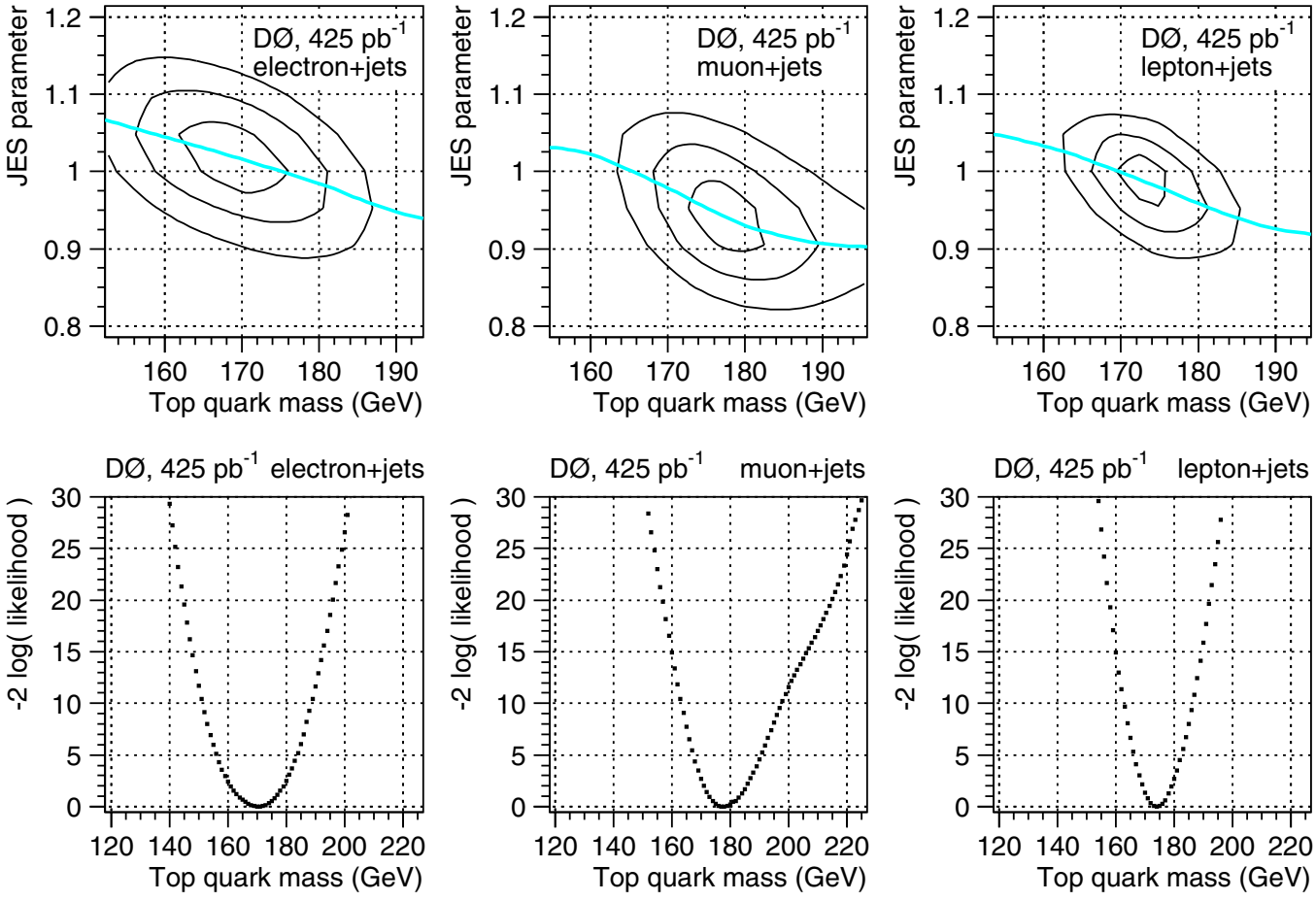

FIG. 8 (color online). Overall likelihood curves for the events observed in data, in the electron+jets channel (left), muon+jets (middle), and both channels combined (right). The top plots show the full 2-dimensional likelihood as a function of the jet energy scale parameter (JES) and top quark mass. Each contour, n, corresponds to a difference in likelihood of $\Delta \ln(\mathcal{L}) = -n^2/2$ with respect to the maximum likelihood. The fitted value of the JES parameter as a function of the top quark mass is plotted as the gray line superimposed on the 2D likelihoods. The bottom plots show the likelihood as a function of the top quark mass along the gray line from the upper plots. The fitted values from these distributions have to be corrected for the calibration from MC simulation to obtain the final results.

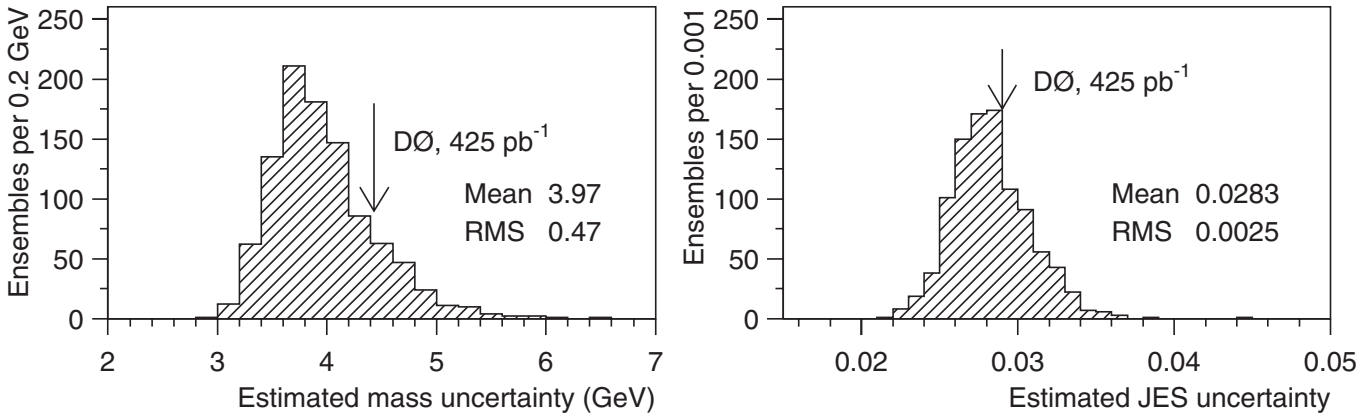

FIG. 9. Distribution of the estimated statistical uncertainty on the top quark mass measurement (left) and JES measurement (right) for the fully calibrated analysis, in the combined lepton+jets channel. The values observed in data are indicated by the arrows.

$0.962^{+0.021}_{-0.023}$, where the uncertainties correspond to the combined statistical and systematic bounds from the jet+photon studies. This is consistent with the value of 0.989 ± 0.029 measured *in situ*.

X. SYSTEMATIC UNCERTAINTIES

The calibration of the analysis relies on Monte Carlo simulation. Therefore any discrepancy between the Monte Carlo simulation and the data may lead to a bias and thus to a systematic shift in the measured top quark mass. In this section we describe the aspects of the simulation which may not accurately represent the data and evaluate the possible effect on the mass measurement. To determine the impact of each uncertainty, we perform ensemble tests using a pool of simulated events that are modified according to the uncertainty in question. The shift in the mean fitted ensemble mass compared to the default value gives the size of the corresponding systematic uncertainty.

The total systematic uncertainty on the top quark mass measurement is obtained by adding all contributions in quadrature. The following sources of systematics are considered (also see Table V):

(i) *Jet energy scale p_T dependence.*—The inclusion of a uniform jet energy scale parameter JES as a free parameter in the mass fitting and calibration procedure ensures that a relative difference in overall jet energy scale between data and Monte Carlo is corrected for. The corresponding uncertainty is included in the quoted statistical (stat+JES) uncertainty. Any residual discrepancy between data and Monte Carlo jet energy calibration that cannot be described by a uniform scale factor may lead to an additional systematic error on the top quark mass. The largest additional effect is expected from the uncertainty in the jet-p_T dependence [7]. The size of the impact of a possible jet-p_T dependent shape is estimated by scaling the energies of all jets in the MC with a factor $(1 + 0.02\frac{p_T^{\text{jet}} - 100\ \text{GeV}}{100\ \text{GeV}})$, where p_T^{jet} is the default reconstructed jet p_T. The value of 0.02 is suggested by the jet+photon studies. The mass obtained with the modified pseudoexperiments is compared to the default result and the shift of 0.45 GeV is quoted as a systematic uncertainty.

(ii) *Jet reconstruction efficiency and resolution.*—In addition to uncertainties on the reconstructed jet energies, differences between data and the Monte Carlo simulation in the jet reconstruction efficiency and jet energy resolution may lead to a mass bias. Both efficiency and resolution are varied as a function of jet p_T and rapidity within estimated uncertainties. No significant effect is observed, with an estimated statistical precision of 0.15 GeV. For both effects combined, a systematic uncertainty of 0.22 GeV is quoted.

TABLE V. Summary of systematic uncertainties.

Source of uncertainty	Size of the effect (GeV)
Jet energy scale (p_T dependence)	0.45
Jet ID efficiency and resolution	0.22
b fragmentation	1.30
b response (h/e)	1.15
b tagging	0.29
Trigger uncertainty	$+0.61 - 0.28$
Signal modeling	0.73
Signal fraction (stat+sysstat + sys)	0.12
Background modeling	0.20
Multijet background	0.28
MC calibration	0.25
PDF uncertainty	0.023
Total systematic uncertainty	$+2.10 - 2.04$

(iii) *b-fragmentation.*—While the overall jet energy scale uncertainty is included in the statistical uncertainty from the fit, differences between data and Monte Carlo in the ratio of b-jet and light-jet energy scale could still affect the measurement. One possible source for such differences could be the description of b-jet fragmentation in the simulation. To estimate the uncertainty from this source we used samples of simulated $t\bar{t}$ events with different fragmentation models for b jets. The default Bowler [25] scheme with $r_b = 1.0$ is replaced with $r_b = 0.69$ or with Peterson [26] fragmentation with $\varepsilon_b = 0.001\,91$. These parameter values were obtained by tuning PYTHIA simulation to LEP data [27–29]. The size of the variation in r_b corresponds to a larger shift in mean scaled energy $\langle x_B \rangle$ of b hadrons than the uncertainties reported in [27–30]. The comparison between the Bowler and Peterson scheme addresses the uncertainty on the shape of the x_B distribution. Ensemble tests are repeated using events from each of the three simulations. The absolute values of the deviations in top quark mass results with respect to the standard sample are added in quadrature and quoted as a symmetric uncertainty of 1.3 GeV.

(iv) *b-jet energy response.*—Uncertainties in the simulation of the ratio between the calorimeter response to hadronic showers and electromagnetic showers (h/e ratio) may lead to additional differences in the b/light jet energy scale ratio between data and simulation. The possible size of the effect is studied in simulation, combining the uncertainty in the modeling of h/e calorimeter response ratio with the difference in particle content between light-quark and b jets. An estimated uncertainty of 1.4% on the b/light jet energy scale ratio is found. Ensemble tests show that this corresponds to a systematic uncertainty on the top quark mass of 1.15 GeV.

(v) *b-tagging.*—The b tagging rates for b jets, c jets, and light-quark jets are varied within the uncertainties known from the data, and the resulting variations are propagated to the final mass results. Uncertainties in the heavy flavor composition of the background are also considered. The combined effect is 0.29 GeV.

(vi) *Trigger.*—The trigger efficiencies in the Monte Carlo simulation are varied by their uncertainties estimated from data. The resulting variations in fitted mass are summed in quadrature, leading to a combined trigger uncertainty of $+0.61 - 0.28$ GeV.

(vii) *Signal modeling.*—The main uncertainty in the modeling of $t\bar{t}$ events is related to the radiation of gluons in the production or decay of the $t\bar{t}$ system. A difference in the description of hard gluon radiation could affect the transverse momentum spectrum of the $t\bar{t}$ system or, for example, change the rate of misassignment of gluon jets to the quarks from the hadronically decaying W boson, which could affect the reconstructed top quark mass. To assess the uncertainty related to the modeling of high energy gluons, the difference is studied between the default signal simulation and a dedicated $t\bar{t}$+jet simulation in which an energetic parton is produced in addition to the $t\bar{t}$ system in the production process simulated by ALPGEN. It is estimated that in the class of events that pass the full event selection, the fraction of simulated events with such an energetic gluon disagrees with the data by less than 35%. Pseudo-experiments are made with the usual sample composition, but replacing the default $t\bar{t}$ events with the events from the dedicated $t\bar{t}$+jet simulation. 35% of the observed shift in the fitted mass corresponds to 0.73 GeV, which is assigned as a systematic uncertainty.

(viii) *Signal fraction.*—Since the $t\bar{t}$ fraction f_{top} is fitted together with the top quark mass and the JES parameter, the mass measurement is affected by the uncertainty on the signal fraction in the data sample. We estimate two sources of systematic uncertainty: a variation of the signal fraction in the ensemble test used to calibrate the method and the effect of a possible systematic offset in the fitted signal fraction with respect to the true signal fraction internally in the mass fit.

We take the 7% relative statistical uncertainty of the signal fraction found by combining the μ+jets and e+jets numbers shown in Table II. We add in quadrature an estimated relative systematic uncertainty of 11% estimated from the cross section measurements [17]. New ensemble tests for the calibration procedure are performed with the mean of the Poisson distribution (for the signal fraction) shifted by $(11 \oplus 7)\%$. Following this procedure the combined fit will still correctly fit the different signal fraction and compensate for the effect. This does not take into account the effect of a possible systematic discrepancy between the data and the Monte Carlo model of signal and background, which could lead to a systematic bias in the fitted signal fraction. To evaluate this additional systematic, the mass fit is forced to systematically overestimate or underestimate the $t\bar{t}$ fraction by 11% (with respect to the value preferred by the likelihood fit), and the shift in fitted mass is quoted as a systematic uncertainty. The combined uncertainty, adding the

above two contributions in quadrature, is 0.12 GeV.

(ix) *Background modeling.*—The sensitivity of the measurement to the choice of background model is studied by comparing two enlarged pseudoexperiments in which the background simulation is changed. One sample is based on the standard W+jets simulation using a factorization scale of $Q^2 = M_W^2 + \sum_j (p_T^j)^2$ while in the other pseudoexperiment a sample of W+jets events is used that are generated with a different factorization scale of $Q'^2 = \langle p_T^j \rangle^2$. The observed difference in fitted mass is 0.20 GeV which is assigned as a systematic uncertainty.

(x) *QCD multijet background.*—In the calibration procedure, the W+jets simulation is used to model the small multijet background in the selected data sample. To study the systematic uncertainty due to this approximation, we selected a dedicated multijet-enriched sample of events from data by inverting the lepton isolation cut in the event selection. The calibration of the method is carried out with pseudoexperiments in which these events are used to model the multijet background, according to the fractions given in Table II. The observed shift is 0.28 GeV, which is quoted as a systematic uncertainty.

(xi) *MC calibration.*—The statistical uncertainty on the calibration curves shown in Fig. 6 is propagated through the analysis and yields a systematic uncertainty on the result of 0.25 GeV.

(xii) *Uncertainty due to the parton distribution functions (PDF).*—The ideogram analysis measures the top quark mass directly from the invariant mass of the $t\bar{t}$ decay products without making specific assumptions regarding the production process. Nevertheless, the calibration of the analysis relies on Monte Carlo simulation in which a certain PDF set was used (CTEQ5L [31]). It is conceivable that a different choice of PDFs would lead to a slightly different calibration. To study the systematic uncertainty on the top quark mass due to the precise PDF description, several PDF uncertainties are considered. PDF variations provided with the next-to-leading-order PDF set CTEQ6M [32] are compared to the default CTEQ6M. The difference between CTEQ5L and MRST [33] leading order PDFs is taken as a separate contribution. Also the effect of a variation in α_s is evaluated. In all cases a large pseudoexperiment composed of events generated with CTEQ5L is reweighted so that distributions corresponding to the desired PDF set are obtained. The difference between weighted and unweighted pseudoexperiments is then quoted as systematic uncertainty, and all individual uncertainties are added in quadrature. The resulting combined uncertainty is found to be very small: ± 0.02 GeV.

XI. CROSS-CHECK USING AN EXTERNAL JES CONSTRAINT

As a cross-check, the analysis is repeated using the two alternative JES fitting strategies discussed in Sec. VIII F. Fixing the JES parameter in the fit and relying fully on the external JES constraint from jet+photon studies, the top quark mass is measured to be

$$m_t = 175.8 \pm 2.9(\text{stat})^{+2.1}_{-2.7}(\text{JES}) \text{ GeV},$$

quoting only the statistical uncertainty (stat) and the systematic uncertainty due to the jet energy scale (JES). In the other alternative approach, the JES parameter is allowed to float freely in the fit but no calibration of the JES slope is applied. Again, the external JES constraint from jet+photon studies is required to set the jet energy scale and the remaining JES systematics. Effectively this approach combines *in situ* with external JES information, leading to the following result:

$$m_t = 173.9 \pm 3.6(\text{stat})^{+1.3}_{-1.0}(\text{JES}) \text{ GeV}.$$

Comparing the last (most precise) cross-check with the main result, one can conclude that omitting the external JES constraint and relying fully on the *in situ* information changes the central result only by 0.2 GeV. The 2 GeV difference between the first cross-check and the main result correlates very well with the 1.1% difference in JES value between the default Monte Carlo scale and *in situ* JES measurements. This difference is fully covered by the quoted uncertainties.

XII. CONCLUSION

The ideogram method has been used for the first time to measure the top quark mass in $t\bar{t}$ events with the ℓ+jets topology. This technique employs a kinematic fit to extract mass information from the events, while improving the statistical sensitivity by constructing an analytic likelihood for every event taking into account all jet permutations and the possibility that the event is background. Lifetime-based identification of b jets is employed to enhance the separation between $t\bar{t}$ signal and background and to improve the assignment of the observed jets to the partons in the $t\bar{t}$ hypothesis. To reduce the systematic uncertainty due to the jet energy scale calibration, an overall scale factor JES for the energy of the reconstructed jets is a free parameter in the fit determined simultaneously with the top quark mass and the signal fraction.

From a D0 Run II data sample of approximately 425 pb^{-1}, 116 events are selected in the electron+jets channel and 114 in the muon+jets channel. The top quark mass is measured to be

$$m_t = 173.7 \pm 4.4(\text{stat} + \text{JES})^{+2.1}_{-2.0}(\text{syst})\ \text{GeV}$$

with a fitted JES scaling factor,

$$\text{JES} = 0.989 \pm 0.029(\text{stat only}),$$

which is consistent with the reference jet energy scale ($= 1.0$) and with the results from the jet+photon calibration ($\approx 0.962^{+0.021}_{-0.023}$). The mass result is in good agreement with the matrix element measurement using the same data set [7] and with other recent top quark mass measurements [4,34].

ACKNOWLEDGMENTS

We thank the staffs at Fermilab and collaborating institutions, and acknowledge support from the DOE and NSF (USA); CEA and CNRS/IN2P3 (France); FASI, Rosatom, and RFBR (Russia); CAPES, CNPq, FAPERJ, FAPESP, and FUNDUNESP (Brazil); DAE and DST (India); Colciencias (Colombia); CONACyT (Mexico); KRF and KOSEF (Korea); CONICET and UBACyT (Argentina); FOM (The Netherlands); PPARC (United Kingdom); MSMT (Czech Republic); CRC Program, CFI, NSERC, and WestGrid Project (Canada); BMBF and DFG (Germany); SFI (Ireland); The Swedish Research Council (Sweden); Research Corporation; Alexander von Humboldt Foundation; and the Marie Curie Program.

[1] F. Abe *et al.* (CDF Collaboration), Phys. Rev. Lett. **74**, 2626 (1995); S. Abachi *et al.* (D0 Collaboration), Phys. Rev. Lett. **74**, 2632 (1995).
[2] ALEPH, DELPHI, L3, OPAL, and SLD Collaborations, LEP Electroweak Working Group, SLD Electroweak Group, and SLD Heavy Flavour Group, Phys. Rep. **427**, 257 (2006).
[3] B. Abbott *et al.* (D0 Collaboration), Phys. Rev. D **58**, 052001 (1998); S. Abachi *et al.* (D0 Collaboration), Phys. Rev. Lett. **79**, 1197 (1997).
[4] A. Abulencia *et al.* (CDF Collaboration), Phys. Rev. D **73**, 032003 (2006); Phys. Rev. Lett. **96**, 022004 (2006).
[5] V. M. Abazov *et al.* (D0 Collaboration), Nature (London) **429**, 638 (2004); J. Estrada, Ph.D. thesis, University of Rochester, 2001, http://lss.fnal.gov/archive/thesis/fermilab-thesis-2001-07.pdf.
[6] A. Abulencia *et al.* (CDF Collaboration), Phys. Rev. D **73**, 092002 (2006).
[7] V. M. Abazov *et al.* (D0 Collaboration), Phys. Rev. D **74**, 092005 (2006); P. Schieferdecker, Ph.D. thesis, LMU München, 2005, http://www-d0.fnal.gov/results/publications_talks/thesis/schieferdecker/thesis.pdf.
[8] P. Abreu *et al.* (DELPHI Collaboration), Eur. Phys. J. C **2**, 581 (1998); Phys. Lett. B **462**, 410 (1999); **511**, 159 (2001); M. Mulders, Ph.D. thesis, FOM and University of Amsterdam, 2001, http://delphiwww.cern.ch/delphd/thesis/mulders/ThesisMulders.ps.gz.
[9] W.-M. Yao *et al.* (Particle Data Group), J. Phys. G **33**, 1 (2006).
[10] T. Aaltonen *et al.* (CDF Collaboration), Phys. Rev. Lett. **98**, 142001 (2007).
[11] V. M. Abazov *et al.*, Nucl. Instrum. Methods Phys. Res., Sect. A **565**, 463 (2006).
[12] S. Abachi *et al.* (D0 Collaboration), Nucl. Instrum. Methods Phys. Res., Sect. A **338**, 185 (1994).
[13] V. M. Abazov *et al.*, Nucl. Instrum. Methods Phys. Res., Sect. A **552**, 372 (2005).
[14] R. E. Kalman, J. Basic Eng. **82**, 35 (1960); R. E. Kalman and R. S. Brucy, J. Basic Eng. **83**, 95 (1961); P. Billoir, Nucl. Instrum. Methods Phys. Res., Sect. A **225**, 352 (1984).
[15] V. M. Abazov *et al.* (D0 Collaboration), Phys. Rev. D **74**, 112004 (2006).
[16] We use the iterative midpoint cone algorithm, as described in Sec. 3.5 of G. C. Blazey *et al.*, in *Proceedings of the Workshop: QCD and Weak Boson Physics in Run II*, edited by U. Baur, R. K. Ellis, and D. Zeppenfeld (Fermilab Report No. Fermilab-Pub-00/297, 2000).
[17] V. M. Abazov *et al.* (D0 Collaboration), Phys. Lett. B **626**, 35 (2005).
[18] M. L. Mangano *et al.*, J. High Energy Phys. 07 (2003) 1.
[19] T. Sjöstrand *et al.*, Comput. Phys. Commun. **135**, 238 (2001).
[20] R. Brun and F. Carminati, CERN program library long writeup, W5013, 1993.
[21] V. M. Abazov *et al.* (D0 Collaboration), Phys. Rev. D **72**, 011104 (2005).
[22] V. M. Abazov *et al.* (D0 Collaboration), Phys. Rev. Lett. **98**, 041801 (2007.
[23] V. M. Abazov *et al.* (D0 Collaboration), Phys. Lett. B **626**, 45 (2005).
[24] B. Efron, SIAM Rev. **21**, 460 (1979); P. Diaconis and B. Efron, Sci. Am. **248**, No. 5, 96 (1983); B. Efron and R. J. Tibshirani, *An Introduction to the Bootstrap* (Chapman & Hall/CRC, New York, 1993).
[25] M. G. Bowler, Z. Phys. C **11**, 169 (1981).
[26] C. Peterson *et al.*, Phys. Rev. D **27**, 105 (1983).
[27] A. Heister *et al.*, Phys. Lett. B **512**, 30 (2001).
[28] G. Abbiendi *et al.* (OPAL Collaboration), Eur. Phys. J. C **29**, 463 (2003).
[29] G. Barker *et al.*, DELPHI conference report, 2002-69 CONF 603.
[30] K. Abe *et al.* (CDF Collaboration), Phys. Rev. Lett. **84**, 4300 (2000).
[31] H. L. Lai *et al.* (CTEQ Collaboration), Eur. Phys. J. C **12**, 375 (2000).
[32] J. Pumplin *et al.* (CTEQ Collaboration), J. High Energy

Phys. 07 (**2002**) 012.
[33] A. D. Martin, R. G. Roberts, W. J. Stirling, and R. S. Thorne, Eur. Phys. J. C **14**, 133 (2000).
[34] A. Abulencia *et al.* (CDF Collaboration), Phys. Rev. Lett. **96**, 152002 (2006); Phys. Rev. D **73**, 112006 (2006); **74**, 032009 (2006); arXiv:hep-ex/0612060; arXiv:hep-ex/0612061; V. M. Abazov *et al.* (D0 Collaboration), arXiv:hep-ex/0609056.